Mechanical heterogeneity in a soft biomaterial niche controls BMP2 signaling

Erik Brauer [a,b,c,**], Aaron Herrera [a,b,c,1], Raphaela Fritsche-Guenther [e,1], Sophie Görlitz [a,b,c], Hans Leemhuis [f], Petra Knaus [b,d], Jennifer A. Kirwan [e], Georg N. Duda [a,b,c], Ansgar Petersen [a,b,c,*]

[a] Julius Wolff Institute, Berlin Institute of Health at Charité - Universitätsmedizin Berlin, Germany
[b] Berlin School for Regenerative Therapies, Charité – Universitätsmedizin Berlin, Germany
[c] BIH Center for Regenerative Therapies, Berlin Institute of Health at Charité – Universitätsmedizin Berlin, Germany
[d] Freie Universität Berlin, Institute for Chemistry and Biochemistry, Berlin, Germany
[e] BIH Metabolomics Platform, Berlin Institute of Health at Charité – Universitätsmedizin Berlin, Berlin, Germany
[f] Matricel GmbH, Herzogenrath, Germany

ARTICLE INFO

ABSTRACT

The extracellular matrix is known to impact cell function during regeneration by modulating growth factor signaling. However, how the mechanical properties and structure of biomaterials can be used to optimize the cellular response to growth factors is widely neglected. Here, we engineered a macroporous biomaterial to study cellular signaling in environments that mimic the mechanical stiffness but also the mechanical heterogeneity of native extracellular matrix. We found that the mechanical interaction of cells with the heterogeneous and non-linear deformation properties of soft matrices (E < 5 kPa) enhances BMP-2 growth factor signaling with high relevance for tissue regeneration. In contrast, this effect is absent in homogeneous hydrogels that are often used to study cell responses to mechanical cues. Live cell imaging and *in silico* finite element modeling further revealed that a subpopulation of highly active, fast migrating cells is responsible for most of the material deformation, while a second, less active population experiences this deformation as an extrinsic mechanical stimulation. At an overall low cell density, the active cell population dominates the process, suggesting that it plays a particularly important role in early tissue healing scenarios where cells invade tissue defects or implanted biomaterials. Taken together, our findings demonstrate that the mechanical heterogeneity of the natural extracellular matrix environment plays an important role in triggering regeneration by endogenously acting growth factors. This suggests the inclusion of such mechanical complexity as a design parameter in future biomaterials, in addition to established parameters such as mechanical stiffness and stress relaxation.

1. Introduction

In situ tissue engineering (TE) aims to overcome the current limitations of treatment strategies to induce regeneration in cases where current treatment therapies fail. So far, a gold standard to treat e.g. non-unions or spinal fusions is by using Bone Morphogenetic Proteins (BMPs) [1–3]. Beyond their function as bone inducing morphogens, BMPs are recognized for their manifold function in the entire human body during processes of embryogenesis and organogenesis as well as their role in regeneration and disease [4,5]. Since BMPs lose their activity very quickly under physiological conditions, supraphysiological concentrations must be administered when applied clinically. This may lead to side effects such as increased inflammation, infection and callus swelling [6]. To allow lower dosing of BMPs, distinct bone TE strategies focus on an enhanced release kinetics via stronger adsorption [7–9] or covalent immobilization [10–12] of the ligand. However, this ignores the general effect these materials themselves have on cellular behavior due to their surface functionalization, porosity, mechanical properties and geometry

* Corresponding author. Julius Wolff Institute, Berlin Institute of Health at Charité - Universitätsmedizin Berlin, Germany.
** Corresponding author. Julius Wolff Institute, Berlin Institute of Health at Charité - Universitätsmedizin Berlin, Germany.
*E-mail address:* ansgar.petersen@bih-charite.de (A. Petersen).
[1] Authors contributed equally.

[13–15] as well as how cells sense and convert the BMP stimulus differently in response to such environmental cues.

Increasing evidence highlights the modulatory role of mechanical forces in BMP signaling. Mechanical loading increases signaling via the BMP-activated transcription factor Smad in osteoblasts [16] and promotes BMP-mediated *in vivo* healing outcomes [17,18]. Moreover, fluid shear stress regulates BMP signaling in endothelial cells [19–21] and even osteoblasts [22]. While immediate short term effects of mechanical stimulation may be mediated by interaction of BMP receptors with integrins [23], long term load-induced osteogenic differentiation of progenitor cells relies on the autocrine stimulation via BMP2 [24]. While the significant impact of stiffness on the differentiation of mesenchymal

progenitor cells is well known [13], how stiffness affects BMP signaling remains elusive. Some studies suggest a stronger BMP pathway activation with higher substrate stiffness [25,26], others a stiffness-dependent cooperation with mechano-responsive YAP/TAZ signaling on a transcription level [27]. However, these studies mostly oversimplify the extracellular environment and study cell responses on very soft 2D substrates with non-physiological stiffness [E < 0.5 kPa] that leads to aberrant, unphysiological cell rounding. Such rounding due to increased integrin receptor internalization is caused by the specific hydrogel porosity, which leads to weak adhesion molecule binding to the underlying biomaterial [28]. In contrast, a recent study demonstrated an increased BMP-mediated alkaline phosphatase activity in a soft
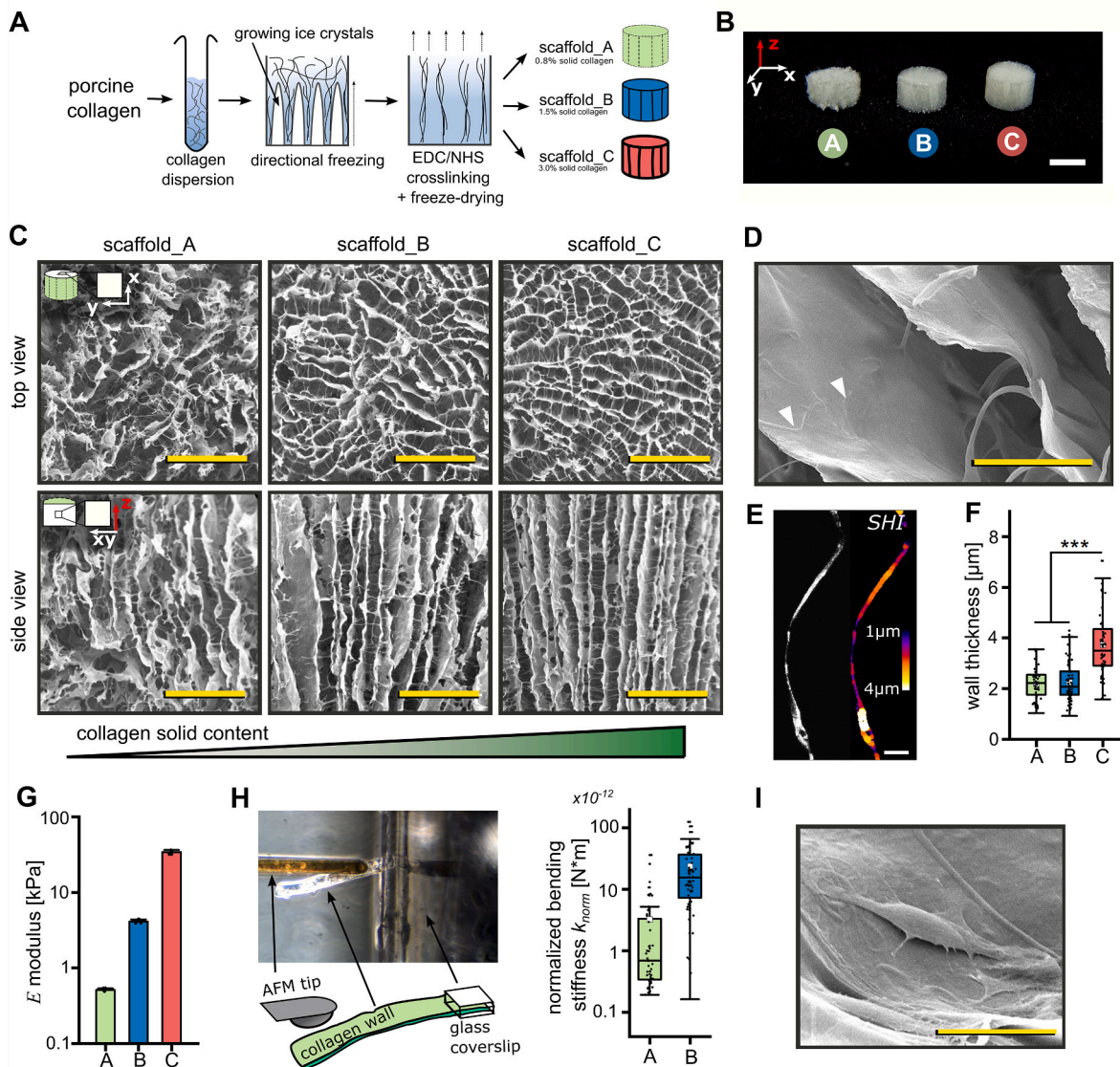
Fig. 1. Fabrication of macroporous 3D collagen scaffolds. (A) Schematic representation of the biomaterial manufacturing process through directional freezing and subsequent freeze-drying. The 3D scaffolds were prepared with a solid collagen content of 0.8 wt% [scaffold_A], 1.5 wt% [scaffold_B] and 3.0 wt% [scaffold_C]. **(B)** Image of all three collagen scaffolds. The samples were punched out of 30 × 40 × 3 mm sheets with a biopsy punch (Ø 5 mm). Scale bar 3 mm. **(C)** Scanning electron microscopy (SEM) of the cylindrical scaffolds from above (top surface in the top row) and from the side (mantle surface in the bottom row). Scale bar 500 μm. **(D)** SEM image of individual walls with visible topological variations (white arrows). Scale bar 50 μm. **(E)** single confocal plane of a collagen wall cross section visualized by Second Harmonic Generation Imaging (SHI). Thickness indication via the BoneJ plugin function from ImageJ [33]. Scale bar 10 μm. **(F)** Quantification of the scaffold wall thickness using high-resolution SHG images. N > 50 of at least 2 independent samples. **(G)** Young's Modulus E of macroporous collagen scaffolds: scaffold_A: 0.5 kPa, scaffold_B: 4.1 kPa, scaffold_C: 34 kPa. N = 3. **(H)** Quantification of scaffold wall bending stiffness k_{norm} using Atomic Force Microscopy. Segments (cantilever beams) of the collagen scaffold walls were prepared and mounted between two glass slides. Cantilever beam bending under controlled force application was recorded to calculate cantilever stiffness (N/m) that was corrected for the individual cantilever width and length to obtain a normalized bending stiffness (N*m). For details see materials and methods. N > 48 (Data re-analyzed from [31]) **(I)** Cryo-SEM of fixed scaffolds seeded with human fetal osteoblasts after 48 h of culture. Scale bar 20 μm. Statistics via the Mann–Whitney *U* test (two-sided). Significance levels are indicated as: ***p < 0.001.

macroporous 3D material compared to stiffer versions [29]. These discrepancies make it clear that the results in terms of cell adhesion, cell morphology and differentiation are highly dependent on the choice of biomaterial platform [28]. Therefore, the interaction between collagen-based biomaterials and surgically administered BMPs is still unknown. In general, biomaterials can exhibit competencies through a bio-inspired, structured architecture that locally affect the properties of the cell niche [30,31]. In contrast to the extracellular matrix (ECM), homogenous hydrogels lack such local architectural features and competences. Highly organized and architectured biomaterials may be generated by a freezing and freeze-drying process of collagen that can also be used to modify their architectural and mechanical properties [32] without affecting cell adhesion and spreading [31].

With this study, we provide evidence that soft structured biomaterials with mechanical properties in the range of human fracture hematoma are locally deformed by cellular tensile forces while stiffer versions remain un-deformable. This deformation is mostly driven by a highly motile sub-population of cells which can be sensed by more static, neighboring cells. This creates a mode of cellular (self-)stimulation further affecting fundamental processes such as mechano-sensation and metabolism and ultimately inducing growth factor signaling with high relevance for tissue regeneration, such as exemplified here for BMP2 signaling.

2. Results

2.1. Engineering of macroporous scaffolds with variable mechanical stiffness

Porous material niches provide the capability for cells to spread and migrate in three dimensions. We fabricated macroporous collagen scaffolds by a directional freezing and freeze-drying process to mimic the mechanical properties either of an early hematoma or more mature, stiffer tissues (Fig. 1A) [32]. This was achieved by varying the solid content of collagen in the initial dispersion from 0.8% (wt./wt., scaffold_A) to 1.5% (scaffold_B) and 3.0% (scaffold_C). In contrast to collagen solutions used for the generation of collagen gels, the dispersion is characterized by a strong heterogeneity in fiber/fragment size ranging from small to large objects featuring a fiber thickness of up to 3 μm (Supplementary Fig. 1A).

All resulting biomaterials had a similar architecture and consisted of interconnected, channel-like pores oriented along the freezing direction (Fig. 1C, side view) and an isotropic pattern of domains with a local pore orientation lateral to the freezing direction (Fig. 1C, top view). In line with our recent observations [31], the biomaterial with the lowest solid collagen content (scaffold_A) showed a higher intrinsic corrugation of the scaffold walls compared to scaffold B and C. This might be due to the lower density of stabilizing wall-interconnecting struts and a reduced wall thickness (Supplementary Fig. 1B). All biomaterials were similar in pore diameter, highlighting the common underlying architecture (Supplementary Fig. 1C).

On a local level, the material provided a homogenous and continuous surface with local topographical variations (hump-like elevations) (Fig. 1D). The manufacturing by directional freezing and freeze-drying induces a phase separation of the collagen from the solvent which results in thin sheets similar to the production of paper. The topographical variations are the result of the fiber heterogeneity in the original dispersion in which larger fiber fragments are thicker than the wall thickness. Consequently, the material thickness strongly varied even over smaller distances of 10 μm between 1 μm and up to 4 μm (scaffold B, Fig. 1E and F).

We performed mono-axial compression testing to evaluate the effect of the increasing solid collagen content on the mechanical properties of the biomaterial (Fig. 1G). Scaffold_A was the softest with a stiffness (measured by compression along the pore direction) of 0.5 kPa, while scaffold_B exhibited a value of 4.1 kPa and scaffold_C a value of 34 kPa.

Bulk compression allows the measurement of macroscopic mechanical properties, however, in the context of porous materials with an already observed heterogeneity in wall thickness this does not represent the local mechanical properties on the length scale of single cells (~100 μm). Using atomic force microscopy we previously characterized the local mechanical bending stiffness of the collagen scaffold walls [31]. From these values we calculated the normalized bending stiffness (k_{norm}) for the collagen walls that is independent of the geometry (width and length) of the cantilever beam (Fig. 1H). The normalized bending stiffness depends on the local thickness of the scaffold wall (in the third power), the local Young's modulus of the scaffold wall material and additional geometric deviations from the idealized cantilever geometry i.e. the waviness of the scaffold wall. The large variation of the bending stiffness obtained from these measurements confirmed the strong local mechanical heterogeneity of the material with values between 1.9×10^{-13} N*m and 3.6×10^{-11} N*m (variation coeff. 2.04) for scaffold_A and 1.6×10^{-13} N*m and 1.3×10^{-10} N*m (variation coeff. 1.03) for scaffold_B. It was not possible to obtain the according data for scaffold_C as the high density of struts in this scaffold type did not allow a controlled AFM tip approach. The high density of struts prevented measurement of individual walls for scaffold_C. Based on our previously published finite element model of the scaffold, values of bending stiffness are proportional to the mean wall thickness and strut density [31] and can be estimated to be stiffer by a factor of 3 for scaffold_C compared to scaffold_B with a similar degree of intrinsic heterogeneity.

We furthermore initially assessed cell adhesion and observed flat spreading of cells on thin, flat walls similar to a 2D surface which suggests that, aside of local topological variations, cells mostly experience a quasi 2D-like geometry (Fig. 1I).

2.2. BMP response is controlled by biomaterial scaffold stiffness

We quantified the BMP response of human fetal osteoblasts (hFOBs), a model system to analyze BMP signaling [16], in the three 3D collagen scaffolds, benchmarked against collagen-coated polyacrylamide (PAAm) gels as a well-established substrate with inert, homogenous and linearly elastic material properties [34]. The stiffness of these gels was chosen to match the cell-effective stiffness of the collagen materials which can be derived from the macroscopic stiffness through our finite element model [31]. Following this approach, the cell effective stiffness of the scaffolds is 6.4 times higher than the macroscopic stiffness that was measured by compression testing (Fig. 2A). Thus, the cell effective stiffness of our biomaterials was on average 3.2 kPa for the soft scaffold (scaffold_A), 26.2 kPa for the medium soft scaffold (scaffold_B) and 217 kPa for the stiff scaffold (scaffold_C).

To analyze the BMP pathway activation, cells were stimulated with 5 nM BMP2. Phosphorylation of BMP-activated Smad transcription factors was monitored 60 min after BMP2 stimulation (Fig. 2B) across all settings. Smad phosphorylation was increased in the cells on the softest (0.5 kPa E_{bulk}) 3D collagen scaffold compared to those on the two stiffer 3D biomaterials (Fig. 2C). This was in clear contrast to the situation on 2D PAAm substrates where cells on the softest gels (1.8 kPa) showed lower Smad phosphorylation compared to the two stiffer gels in agreement with a recent report [26]. We excluded unspecific BMP2 adsorption to the 3D biomaterial by measuring the activity of free BMP2 in the presence of collagen scaffolds over time which showed no biomaterial-dependent variation in BMP2 activity (Supplementary Fig. 2A). Thus, the differences in BMP pathway activation in the cells on the 3D scaffolds compared to those on the 2D surfaces is not biased by differences in BMP diffusion or adsorption.

To assess the progression of the BMP stimulus along the signaling cascade, we subsequently quantified gene expression levels of known BMP/Smad target genes 6 h after stimulation of the cells with BMP2. In line with Smad phosphorylation, we observed an increased induction of the direct Smad target genes ID1 and ID2 in the cells grown on the softest 3D collagen scaffold compared to the two stiffer ones (Fig. 2E and F). We
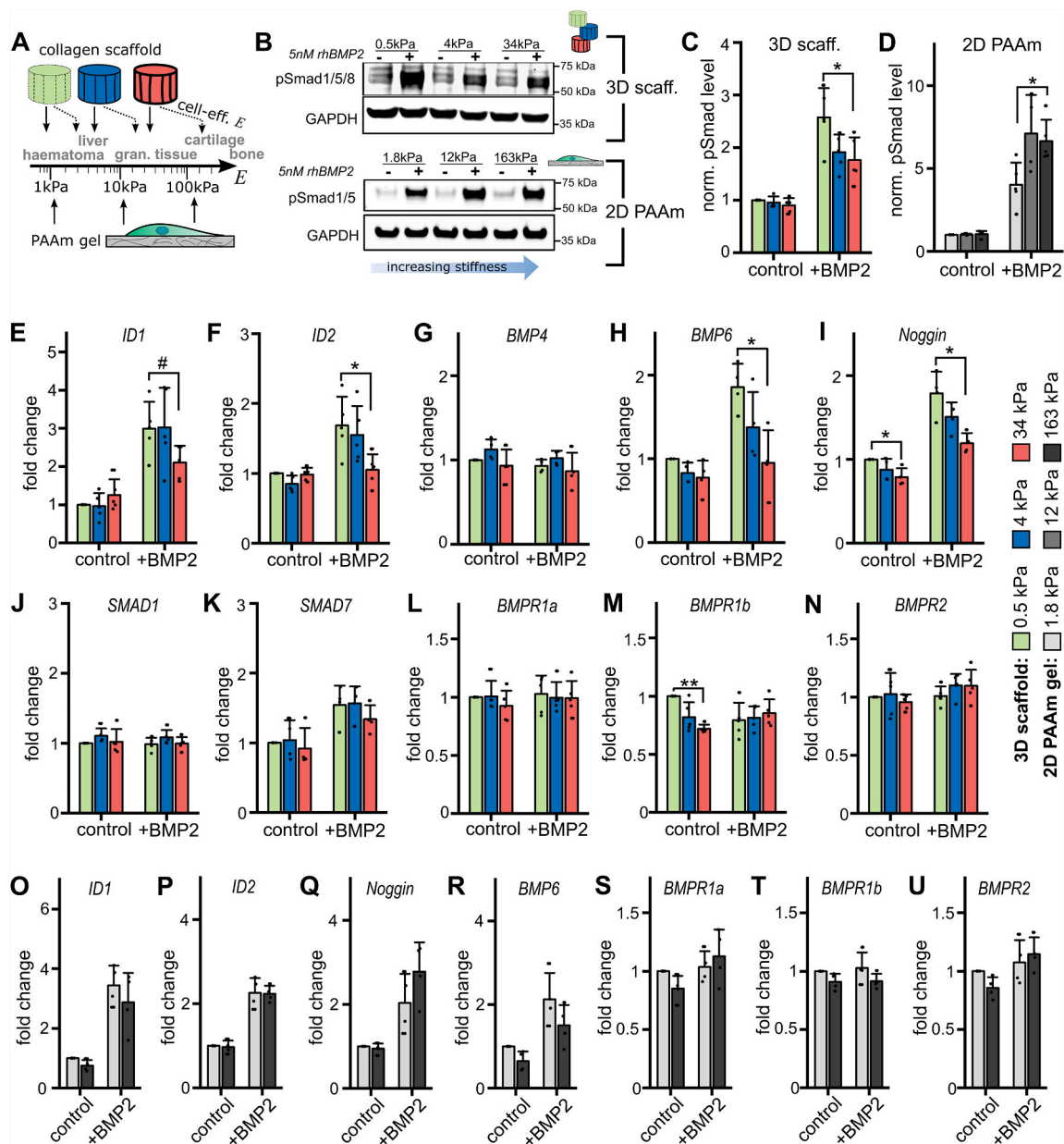
Fig. 2. Stiffness-dependent BMP signaling. (A) Schematic representation of the stiffness range of different tissues compared to the stiffness range of the 3D collagen scaffolds and the 2D PAAm gels. **(B)** Western blot detection of Smad phosphorylation after stimulation of human fetal osteoblasts (hFOBs) with 5 nM rhBMP2. Cells were seeded either in 3D collagen scaffolds or on collagen-coated 2D PAAm gels. GAPDH was used as loading control. **(C)** and **(D)** Quantification of Western blot signals. Signals were normalized to GAPDH signals and expressed as a fold change relative to the unstimulated control of the softest biomaterial (0.5 kPa for 3D collagen or 1.8 kPa for 2D PAAm). N = 4–5. **(E)** to **(N)** Gene expression levels expressed as fold change to the unstimulated control of scaffold a (0.5 kPa, light green). HFOBs were seeded into the macroporous 3D scaffolds and stimulated with 5 nM rhBMP2 for 6 h. N = 4–5. **(O)** to **(U)** Gene expression levels expressed as fold change to the unstimulated control of the softest PAAm gel (1.8 kPa, light grey). HFOBs were seeded onto the 2D PAAm gels and stimulated with 5 nM rhBMP2 for 6 h. N = 4. Statistics via the Mann–Whitney U test (two-sided). Significance levels are indicated as: #p < 0.1, *p < 0.05, **p < 0.01.

further analyzed the gene expression of selected BMPs and the extracellular BMP antagonist Noggin. While BMP4 gene expression did not change, BMP2-mediated induction of BMP6 gene expression was higher in the cells on the softest compared to the two stiffer 3D biomaterials (Fig. 2G and H). The gene expression of the BMP antagonist Noggin was increased in cells cultured on the softest compared to the stiffest 3D scaffold not only in the BMP2 stimulated but also in the unstimulated group (Fig. 2I).

Furthermore, we investigated the regulation of signaling as the BMP cascade is regulated on various levels and depends on the presence of BMP receptors (stimulus sensation), intracellular Smad transcription factors (R-Smad 1, 5 and 8) (stimulus transmission) and inhibitory

Smads (I-Smad 6 and 7) that become activated through BMP stimulation (negative feedback). While R-Smad 1 did not respond to BMP stimulation nor was its transcriptional level affected by stiffness, I-Smad 7 expression was induced by BMP stimulation, but without differences between the three different 3D biomaterials (Fig. 2J and K). However, we observed a significant downregulation of the BMP type 1b receptor in the cells on the stiffest compared to the softest 3D scaffold (Fig. 2M), while the BMP type 1a and BMP type 2 receptors remained unchanged (Fig. 2L and N). This suggests that cells express a stiffness-dependent level of receptors that, in the case of the softest 3D biomaterial, could increase the sensitivity of the cells to BMPs. In clear contrast, we found little difference in BMP target gene expression between cells cultured on

the softest and the stiffest 2D PAAm gel (Fig. 2O-U, Supplementary Figs. 2B–D), and notably there was no difference in BMP receptor expression (Fig. 2S-U).

To assess a potential long-term effect of BMP2 on cell differentiation, we analyzed gene expression levels of primary human mesenchymal stromal/stem cells (hMSCs), known for the multi-lineage differentiation potential, 3 days after BMP2 stimulation (Supplementary Figs. 2E–H). Similar to hFOBs, hMSCs also showed increased ID1 gene expression on the softest compared to the stiffest 3D scaffolds. Additionally, we did not observe large effects both of stiffness and BMP stimulation on the expression of key differentiation factors of osteogenic (Runx2), chondrogenic (Sox9) or adipogenic (PPARγ) differentiation. Since their expression is highly time-point dependent, this suggests, that without further co-stimulation [24], the lineage commitment is not robust in our setup.

Taken together, these data demonstrate not only the stiffness-dependent BMP signaling response, but also the strong influence of the geometrical and architectural properties of the environment presented by the 3D engineered biomaterial compared to 2D substrates that, despite a similar cell-effective stiffness, showed a different stiffness-dependent BMP response.

2.3. Biomaterial architecture influences stiffness-dependent cellular mechanotransduction

To identify potential mechanisms underlying the described cellular BMP response, we compared cellular morphology in the 3D environment with that on the 2D surfaces. HFOBs exhibited a stiffness-independent morphology with a similar spreading behavior in all 3D collagen scaffolds (Fig. 3A–C). In contrast, culturing hFOBs on thin 2D PAAm gels resulted in a smaller and rounder cell morphology on the softest compared to the two stiffer gels. These observations on 2D gels are consistent with previous reports [26,35] describing a smaller, more rounded cell morphology resulting from an enhanced internalization of integrins and BMP receptors in cells grown on very soft 2D gels (0.5 kPa). This was shown to be the result of insufficient ECM molecule tethering on soft PAAm gels [28] which suggests that the decreased Smad phosphorylation of the cells grown on the soft 2D PAAm gels (Fig. 2D, condition "+BMP2", soft vs medium/stiff gel) is strongly influenced by the impaired spreading and adhesion leading to a rounder cell morphology.

To confirm this, we additionally analyzed the BMP signaling response on 2D polydimethylsiloxane (PDMS) substrates which can be tuned in stiffness over a similar range as PAAm gels but due to their bulk material character, ligand anchoring and cell spreading is independent of the materials' elastic modulus [28] (Supplementary Fig. 3A). Here, we did not observe an influence of stiffness (soft: 0.9 kPa vs stiff: 96 kPa) on BMP signaling outcome both, for initial Smad phosphorylation (Fig. 3E and F) and target gene expression (Supplementary Figs. 3B–K) which emphasizes the relevance of a proper cell anchoring and spreading on linearly elastic 2D substrates independent of their substrate stiffness.

Notably, scaffolds with increasing stiffness exhibited an increasing density of collagen struts between the scaffold walls (Supplementary Fig. 1B), which might serve as an additional adhesion site. The struts could promote 3D spanning and lifting of the cells in the stiff scaffold, thereby imposing geometry-dependent effects in addition to the mechanics-dependent effects resulting from the stiffness. We therefore characterized the localization of cellular actin signals relative to the scaffold walls and to the wall-interconnecting struts (Fig. 3G). With increasing stiffness of the 3D scaffolds, we observed an increase in the actin signals near the struts and a decrease in the actin signals near the scaffold walls. In all 3D scaffolds, however, the cells were predominantly located on the scaffold walls (scaffold_A: 83.6%; scaffold_C: 73.6%). Thus, cells might temporarily use the struts to bridge pores to reach neighboring scaffold walls, but they do not reside there permanently.

To further investigate the response of cells to the varying stiffness of the macroporous 3D scaffolds, we analyzed nuclear accumulation of the mechano-sensation marker YAP, whose subcellular localization is controlled by substrate stiffness [36] and accumulates in the nucleus at higher stiffness [35]. We observed a pronounced nuclear accumulation of YAP after 48 h (duration of pre-cultivation) in all 3D scaffolds (Fig. 3H), suggesting that the biomaterial stiffness does not affect the localization of YAP as expected based on literature reports for 2D materials of the same cell-effective stiffness [35,36]. Apart from YAP, the nuclear lamina component Lamin A was regulated by the underlying substrate stiffness and its nuclear protein levels increase with increasing stiffness [37]. Surprisingly, we observed an enhanced level of nuclear Lamin A (fluorescence signal per cell) in FOBs cultured in the softest 3D collagen scaffold that decreased with increasing stiffness (Fig. 3I, Supplementary Fig. 3L). Similarly, and even more pronounced than for nuclear YAP, this finding was the opposite of that reported for cells grown on 2D gels of the same cell-effective stiffness [35] and pointed towards a mechanically active environment in the softest 3D scaffolds.

We have previously demonstrated that a concave geometry reduces nuclear Lamin A protein levels compared to flat or convex surfaces [15]. This might suggest that, within the scaffold, other factors, such as geometry influence cellular YAP and Lamin A levels. Consequently, the observed BMP response might not only be influenced by stiffness, but also by geometry. Although most cells are experiencing a flat, quasi 2D geometry, few cells actively span and lift along such struts (Fig. 3G), which might over-proportionally contribute to the detected mean Smad phosphorylation signal if curvature has a strong influence on this initial signal transduction process. We therefore investigated whether the increased number of strut elements in the stiffer scaffold and the resulting increased tendency of cells to span across the concave regions where struts and walls meet could influence BMP signaling independently of the stiffness. To test this, we analyzed Smad phosphorylation in cells grown on an established geometric platform [15] presenting concave spherical surfaces of different curvature (radius), 60 min after BMP stimulation. However, we did not observe differences in nuclear phospho-Smad levels between cells cultured on concave spherical compared to neighboring flat surfaces (Fig. 3J and K). Although this does not exclude effects of geometry on BMP-induced gene expression, we found no indication that at least the immediate response to BMP stimulation was influenced by geometry. Consequently, more wall-connecting struts are unlikely to explain the stiffness-dependent effects we observed for the 3D biomaterials while they might explain reduced Lamin A levels in the stiffer scaffold. Our findings suggest that the enhanced cell response in the soft scaffold is mediated by more dynamic interactions between the cells and the biomaterial.

This hypothesis was supported by our analysis of the myosin light chain (MLC) regulatory subunit of the acto-myosin motor protein complex (Fig. 3L and M). MLC is activated by phosphorylation and is therefore an indicator of cellular contractility, which is known to increase with substrate stiffness [38]. Consistent with the enhanced Lamin A levels in the soft 3D scaffold and contrary to our expectations, phosphorylation of MLC gradually decreased with increasing scaffold stiffness, suggesting higher mechanical activity of hFOBs cultured in the softest compared to the two stiffer scaffolds.

Taken together, these data suggest a state of enhanced mechanical activity of the cells in the soft 3D scaffold environment that correlates with an enhanced BMP response. These findings are consistently inverse to the described mechano-dependencies of cell contractility, YAP translocation and Lamin A levels of cells grown on 2D polyacrylamide gels [38].

2.4. A soft scaffold environment promotes cellular metabolic activity

Considering that cytoskeletal reorganization and contraction is an energy-consuming process, an increased myosin motor protein activity would require higher metabolic rates to provide the necessary ATP. A
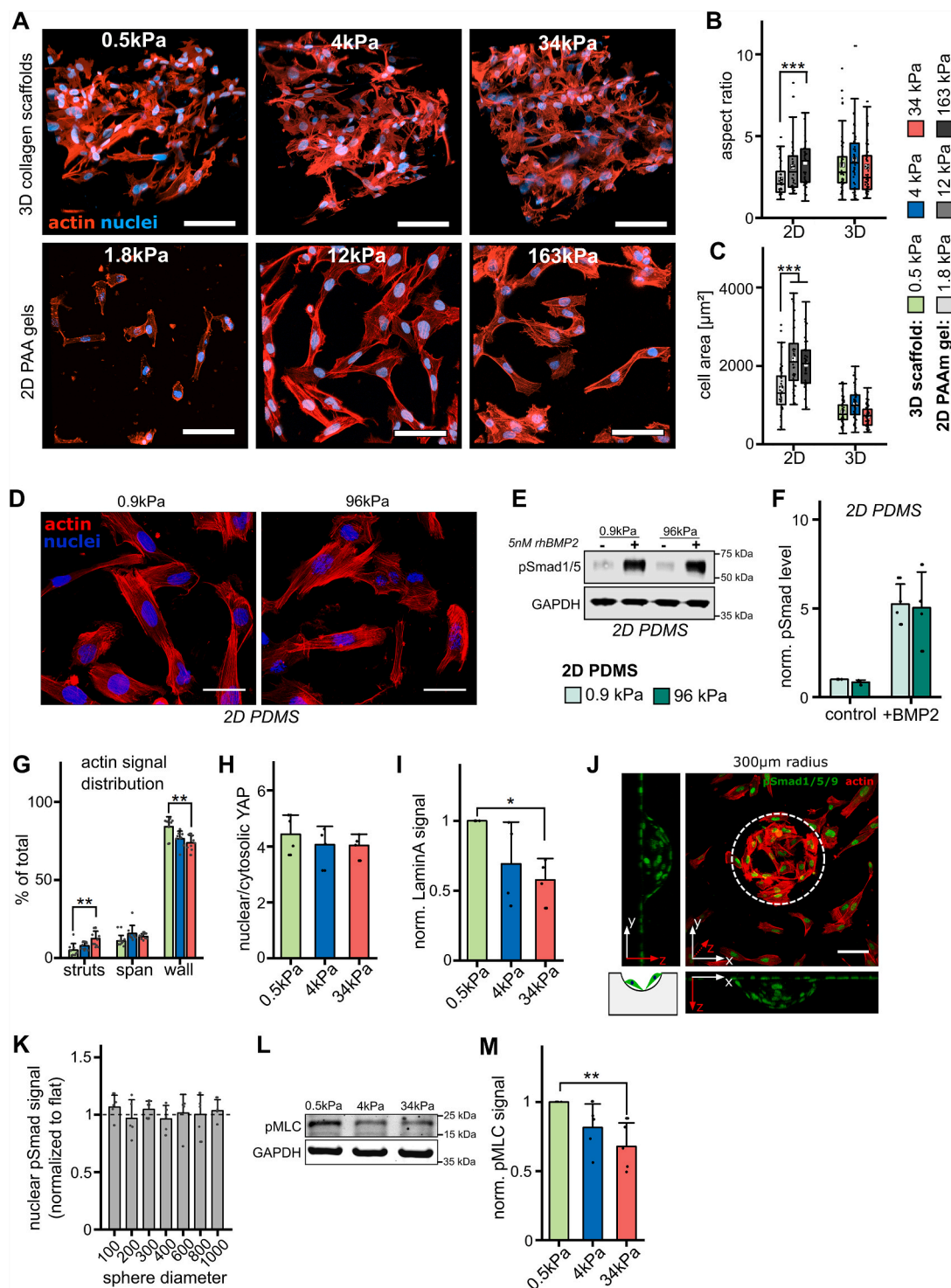
Fig. 3. The influence of biomaterial stiffness and architecture on cell adhesion and morphology: (A) Confocal images of hFOBs either cultured inside 3D macroporous collagen scaffolds (top row) or on top of collagen-coated 2D PAAm gels (bottom row). Scale bar 100 μm. **(B)** Quantification of cellular aspect ratio. N < 50 **(C)** Quantification of cell area. N > 50 **(D)** Confocal Images of hFOBs cultured on top of collagen-coated PDMS substrates (soft, 0.9 kPa, left and stiff, 96 kPa, right). Scale bar 50 μm **(E)** representative Western Blot and **(F)** quantification of relative pSmad signal (normalized to GAPDH as loading control) for hFOBs cultured on top of PDMS stiffness substrates and stimulated with 5 nM BMP2 for 60 min. N = 4.**(G)** Quantification of cellular actin signals co-localizing with SHG signals (either wall-interconnecting struts or walls based on manual segmentation). Actin signals that did not co-localize with SHG signals were regarded as spanning. N = 9 **(H)** Quantification of the ratio of nuclear to cytosolic YAP. N = 4–5. **(I)** Quantification of Lamin A nuclear signal expressed as fold change relative to scaffold a (0.5 kPa). N = 4. **(J)** Confocal image of hFOBs cultured on concave spheres with a radius of 300 μm (white dashed line). Top view (middle) and orthogonal projections of a sphere (bottom: xz; left: yz). The actin cytoskeleton is stained in red and pSmad1/5/9 in green. Scale bar 100 μm. **(K)** Quantification of nuclear pSmad signal in the cells on the spheres, normalized to the pSmad signal of the surrounding cells adhering to a flat surface. N = 3 **(L)** Representative Western Blot and **(M)** Quantification of pMLC signals of hFOBs cultured inside macroporous collagen scaffolds of varying stiffness. N = 4–5. Statistics via the Mann–Whitney *U* test (two-sided). Significance levels are indicated as: *p < 0.05, **p < 0.01, ***<0.001.

recent report highlighted an increased metabolic activity of cells on stiffer compared to soft substrates, which could be linked to the cytoskeletal tensional state of the cells [39]. Since we concluded from our data a higher mechanical activity of the cells on the softest substrate, a potentially higher metabolic activity would further support this interpretation.

To address this point, we performed gas chromatography mass spectrometry (GC-MS) to measure metabolite levels in the cells cultivated in the three different 3D scaffolds (Fig. 4) [40]. Metabolites from the energy-providing metabolic pathways glycolysis and tricarboxylic acid (TCA) cycle were detected at higher levels in the cells cultivated in the two softer scaffolds compared to the stiff scaffold. A similar trend was observed for the amino acids and the glycerol pathway compounds. This might indicate an increased metabolic activity of the cells grown in the soft and medium soft scaffolds. Ribose metabolite pools did not change while a stiffness-dependent decrease was found for Ribose-5-phosphate as part of the pentose phosphate pathway, which converts glucose to NADPH and pentoses as precursors for nucleotide synthesis.

To analyze the general effects on energy metabolism, the metabolites were grouped according to their metabolic class (Supplementary Fig. 4). The combined analysis revealed a significant decrease in metabolites from the TCA cycle and amino acids with increasing scaffold stiffness, while only an insignificant decrease could be observed for glycolysis. This suggests that the cells cultured in the soft scaffold environment, consumed more energy-rich compounds through glycolysis and the TCA cycle, which, similar to the results observed for Lamin A, is contrary to existing literature reports [39]. These data support our hypothesis that an enhanced cellular mechanical activity in soft 3D environments, which is an energy-driven process, leads to increased energy consumption.

2.5. Soft niches promote cell-induced biomaterial deformation

The observed increase in MLC activity and metabolite levels for the soft scaffold suggested a higher cytoskeletal remodeling activity that requires an increased energy consumption and thus metabolic activity. We therefore speculated that this affects the dynamic interaction of the cells with the 3D environment and monitored cellular migration inside the collagen scaffolds by live-cell 3D microscopy (Supplementary videos 1-3). For all three biomaterials, hFOBs showed an active migration within the material without any observable influence of the scaffold stiffness on the overall migration behavior or migration speed (Fig. 5A and B).

Additionally, second harmonic imaging (SHI) was used to visualize the collagen material (Fig. 5C–E). We observed a pronounced, systemic movement of the scaffold walls and the struts of the thin, sheet-like and fiber-like elements of the material in the presence of migrating cells that was the strongest in the softest scaffolds, while the stiffest version did not show such bending and movement (Fig. 5D).

Based on the individual trajectories of wall movement (Fig. 5E), we quantified the magnitude M of scaffold wall deflection that was also highest for the softest scaffold and decreased with scaffold stiffness (Fig. 5F). For a more in-depth characterization of the biomaterial deformation, we converted the biomaterial deflection of individual walls into values of local material strain ($\varepsilon = \Delta L/L$) and analyzed the occurring strains over time (Fig. 5G). We observed compression and stretching occurring simultaneously, indicating temporary and reversible (elastic) material deformation of the biomaterial due to dynamic forces applied by the cells. This suggests that deformations are not synchronized on a larger scale where a dominant occurrence of compressive deformation would indicate macroscopic material contraction and dominant stretching would indicate material swelling. A similar observation was made when calculating material strains between neighboring walls mediated by the wall-interconnecting struts (Supplementary Fig. 5A) where local compression and stretching

occurred simultaneously and intermittently.

In order to determine whether occurring material strains are relevant to and can be sensed by the adhering cells, we determined the maximum strain (ε_{max}) and analyzed it on a more local level in the range of a cell-spanning length (d_1, Fig. 5H). We defined the cell-spanning length as the length of the cell body along the major cell axis, which ranged between 42 and 104 μm (Supplementary Fig. 5B and 5H – grey box). For all biomaterial stiffnesses, the maximum material strain decreased exponentially with the reference distance and reached an equilibrium at around 400 μm with no further decrease. This again underlines the local non-synchronized nature of the occurring strain patterns, since in a spatially synchronized deformation the strain magnitude would be constant for different reference lengths (Fig. 5I). Most importantly, the highest material strains were detected at distances that cells typically span and were significantly increased in the soft material (Supplementary Fig. 5C). A similar pattern was also observed when determining strains occurring between adjacent collagen walls, suggesting that such deformations can also be sensed along wall interconnecting struts (Supplementary Fig. 5D).

Remarkably, not only the magnitude of strains occurring at the cell-spanning length, but also its heterogeneity decreased with increasing stiffness (variation coefficient for material strain ε(cell-span) 0.51 for soft vs. 0.44 for stiff). This observation is in line with our initial mechanical biomaterial characterization by AFM that showed a high variability in the individual wall bending stiffness. This implies that cells experience the walls of the stiff scaffold as generally non-deformable as most walls are above a critical threshold at which cells are no longer capable to efficiently bend the material. In contrast, the stiffness of the soft scaffold was low enough to permit pronounced cell-induced deformation at soft locations of the spatially heterogeneous architecture, while material deformation remained low at other, more stiffer regions. During migration, cells oscillate between such softer, deformable and stiffer, less deformable locations and experience the mechanical heterogeneity of the material. This creates an environment where cells are constantly challenged to adapting their cytoskeletal tension to the strong heterogeneous mechanical properties of the underlying material.

To test the relevance of material heterogeneity for the cell signaling response we eliminated large insoluble fibers from the dispersion by straining through a mesh with a pore size of 5 μm and created a thin gel through simple smearing of the dispersion on top of glass cover slips. Crosslinking was performed through drying either at room temperature or under vacuum at 100 °C for 24 h (Fig. 5J). This resulted in homogenous soft (4.5 kPa) and stiff (27 kPa) gels of the same raw materials as the collagen scaffolds (Fig. 5K). The stiffness measured by AFM-indentations matched the cell-effective stiffness of the soft (3.2 kPa, cell-eff. E-mod) and medium (25.6 kPa, cell-eff. E-mod) stiffness scaffolds where differences in the BMP signaling but also deformation were visible. Remarkably, we did not observe differences in the Smad phosphorylation for soft and stiff collagen gels (Fig. 5L and M). This underlines the relevance of the material heterogeneity and the resulting dynamic deformation behavior for the observed effects on Smad phosphorylation.

Taken together, although cell migration was not affected by the biomaterial's stiffness, the range of macroscopic scaffold stiffness investigated here allowed for pronounced scaffold wall deformation within the softest scaffold, but strongly decreased at the highest macroscopic scaffold stiffness. The strong heterogeneity of the observed strains on the length scale of cells suggests that cells constantly experience changing effective substrate stiffness when moving through the material. This might represent a mode of cellular mechano-(self)stimulation. The resulting continuous mechanical adaptation of cells is proposed to be causative for the observed increase in cell response to BMP, similar to extrinsically applied mechanical load, as elimination of heterogeneity and non-linear deformation abolished the effect on the signaling.
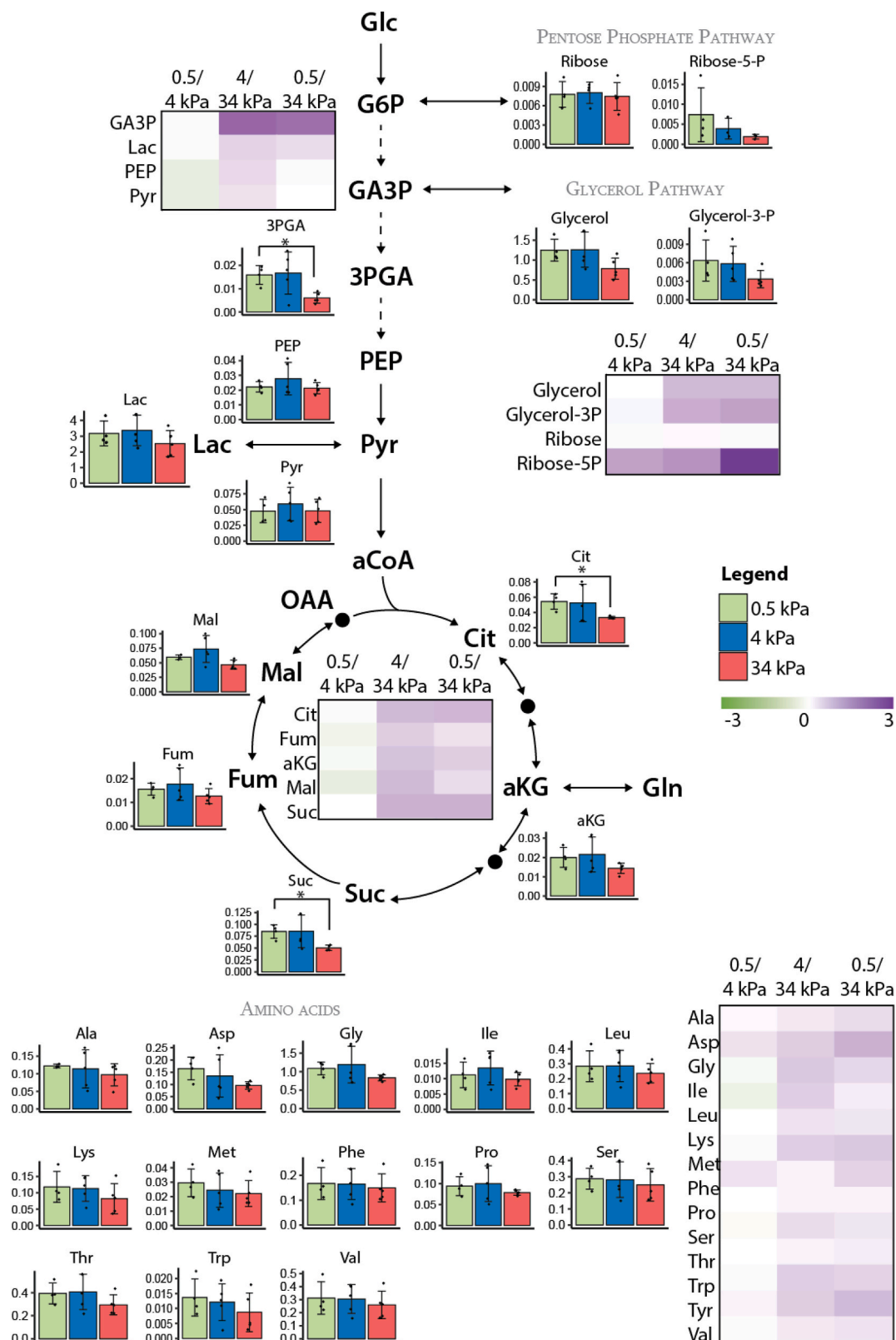
Fig. 4. Metabolic pathway alterations in response to biomaterial stiffness. Levels of metabolites of glycolysis, tricarboxylic acid cycle, glycerol, pentose phosphate pathway and amino acids extracted from hFOBs grown in scaffold A (0.5 kPa), B (4 kPa) and C (34 kPa) after 48 h. The bar charts show the mean and standard deviation of the normalized peak areas (arbitrary units). The heat maps indicate the ratios of the log2 normalized peak areas values from central carbon metabolites comparing the 3 scaffolds. 3PGA: glyceric-acid-3-phosphate. aCoA: acetyl-CoenzymeA. Ala: alanine. aKG: alpha-ketoglutaric acid. Asp: aspartic acid. Cit: citric acid. F6P: fructose-6-phosphate. Fum: fumaric acid. G6P: glucose-6-phosphate. GA3P: glyceraldehyde-3-phosphate. Glc: glucose. Gln: glutamine. Glycerol-3-P: glycerol-3-phosphate. Gly: glycine. Glyc: glycerol. Ile: isoleucine. Lac: lactic acid. Leu: leucine. Lys: lysine. Mal: malic acid. Met: methionine. OAA: oxaloacetate. Phe: phenylalanine. PEP: phosphoenol-pyruvic acid. Pyr: pyruvic acid. Pro: proline. Ser: serine. Suc: succinic acid. Thr: threonine. Trp: tryptophan. Tyr: tyrosine. Val: valine. Ribose-5-P: ribose-5-phosphate. N = 5 Statistics via an unpaired Student's t-test, with a * $p \leq 0.05$.
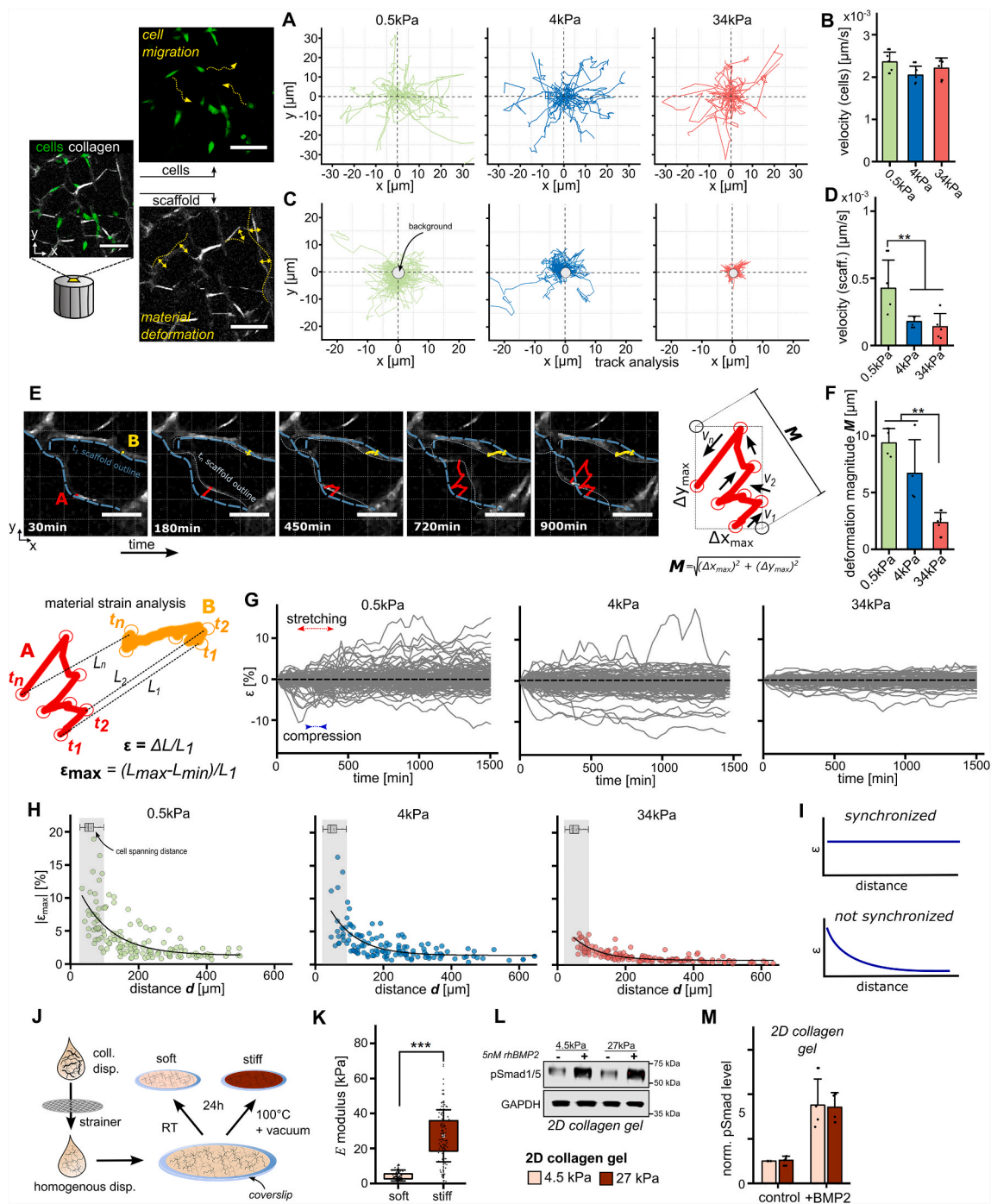
Fig. 5. Cellular migration and traction induces scaffold deformation in a stiffness-dependent manner: (A) Representative time lapse confocal image (scale bar 100 μm) of hFOBs (green, CMFDA dye staining) cultured inside 3D collagen scaffolds (white, second harmonic generation). Trajectory coordinate plots of cells illustrating their migration behavior. **(B)** Quantification of the mean cell migration velocity. N = 4–5. **(C)** Trajectory coordinate plots of the collagen walls. The grey circle indicates the magnitude of the background signal derived from measurement of cell-free scaffolds. **(D)** Quantification of the mean wall movement velocity. N = 4–5. **(E)** Representative series of SHG images illustrating the scaffold deformation over time for selected landmarks (A, red line & B, yellow line). Blue dashed lines illustrate wall shape at 30mins time point. Thin blue dotted line marks the current wall outline for the respective time point. Scale bar 20 μm. **(F)** Quantification of the wall deformation magnitude. N = 4–5. **(G)** Measured biomaterial straining over time relative to reference length at time point 0. A negative value indicates compression, a positive stretching. **(H)** Scaffold strain (maximum linear strain, %) expressed as a function of the reference length. Grey box indicates range of the cell spanning length. **(I)** Schematic display of dependency of occurring strain and reference length for synchronized (e.g. an accordion) and non-synchronized deformation. **(J)** Schematic drawing of the thin collagen gel fabrication process from the original collagen dispersion used for scaffold production. **(K)** Local stiffness of thin collagen gels measured by AFM. N > 50 of at least 3 independent samples. **(L)** representative Western Blot and **(M)** Quantification of relative pSmad signals (fold change) normalized to GAPDH as reference protein for hFOBs after 60 min of stimulation with 5 nM BMP2. The local stiffness corresponds to the cell-effective stiffness of the soft (0.5 kPa) and the medium (4 kPa) stiffness collagen scaffolds (3.2 kPa and 25.6 kPa, respectively). N = 4. Statistics via the Mann–Whitney *U* test (two-sided). Significance levels are indicated as: **p < 0.01, ***<0.001

2.6. Local biomaterial deflection retains BMP synergism at low cell density

From our data, it remained unclear whether the observed amplified BMP response was a consequence of the interaction of individual cells with the material or a consequence of an extrinsic mechanical stimulation resulting from the material deformation caused by neighboring cells (intercellular mechanical stimulation). To understand at what distance the material deformation caused by a single cell can still be perceived by neighboring cells, we analyzed the spatial distribution of the material strain fields by finite element simulation based on a previously established *in silico* model of the biomaterial scaffold wall [31]. Cells were placed at distances of 50, 100, 150, 200 and 300 μm and cell contraction was simulated by thermal material contraction as reported in literature

(Fig. 6A) [41]. Simulations of cell contraction on elastic bulk gels served as controls for analyzing strain distribution patterns (Supplementary Fig. 6A). The stiffness of the bulk gel (3.2 kPa) was chosen to match the cell-effective stiffness of the softest collagen scaffold. While, the elastic bulk hydrogel revealed an isotropic, fast dissipating strain pattern as expected, we observed a partially directed, less defined and non-linear strain pattern emerging on the collagen wall. The wavy character of the collagen scaffold is the critical component for such non-linear strain patterns, because on thin, flat materials the strain patterns were isotropic and more comparable to strain patterns emerging on bulk gels (Supplementary Fig. 6B).

Interestingly, simulations indicated a local strain-induced flattening of the wavy scaffold walls. We recently demonstrated that such a flattening (reduction in the amplitude of wall corrugations)
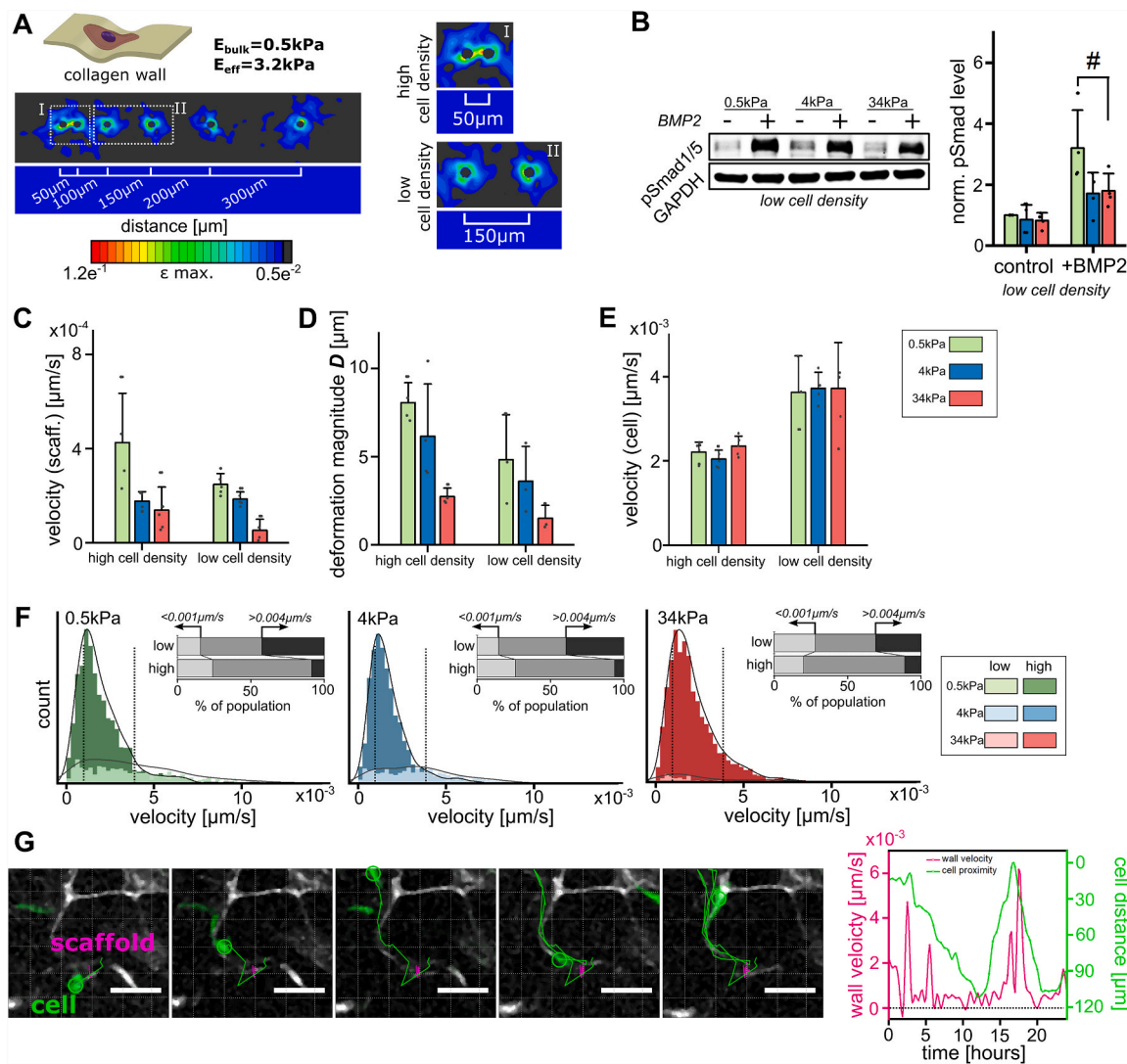
Fig. 6. Local biomaterial straining retains BMP synergism at low cell densities. (A) Finite element simulation of material straining by thermal contraction of a circular cell element at different distances of 50, 100, 150, 200 and 300 μm for soft (E_{bulk} = 0.5 kPa) collagen walls. **(B)** Western blot analysis and quantification of Smad phosphorylation after stimulation of hFOBs stimulated with 5 nM rhBMP2 for 60 min. Cells were seeded in 3D collagen scaffolds at a 10-fold lower cell concentration (500 cells/mm³) compared to the previous experiments. GAPDH was used as loading control Signals were normalized to GAPDH signals and a fold change was formed to the unstimulated control of the soft biomaterial. N = 4. **(C)** Quantification of the velocity of scaffold deformation for the high and the low cell seeding condition. N = 3. **(D)** Quantification of the wall deformation magnitude for the high and the low cell seeding condition. N = 3. **(E)** Quantification of cell migration velocity for the high and the low cell seeding conition. N = 3. **(F)** Distribution of cell migration speeds within high and low cell density populations and fractional shares of stationary (<0.001 μm/s) and highly motile cells (>0.004 μm/s) of the entire cell population which are further indicated by the grey dashed lines. Black lines indicate a kernel density fit function of the histogram. **(G)** Time-laps microscopy of cells (green) and collagen wall (white) for the low cell seeding density in the soft collagen scaffold. Green (cell) and purple (scaffold) lines indicate exemplary trajectories. Scale bar 20 μm. Right: Corresponding quantification of wall velocity (purple) as an expression of biomaterial movement overlaid with measurement of distance to the nearest cell (green) indicating a direct dependency of the migration of an individual cell and biomaterial deformation. Statistics via the Mann–Whitney *U* test (two-sided). Significance levels are indicated as: #p < 0.1

disproportionally increases the cell-effective stiffness [31], suggesting a strain-stiffening response of material to the deformations induced by cell forces. Such a dynamic cell-induced modulation of the mechanical properties of the material is likely to increase the heterogeneity of material properties experienced by the adhering cells.

To understand how close the individual cells are to each other within the biomaterial, we quantified the local cell density from time-lapse imaging data and calculated the corresponding intercellular distance (Supplementary Figs. 6C and D). The average intercellular distance was measured to be in the range of 60–70 μm across all scaffolds. Recent studies suggest that strain values in the range of 0.1%–1% are irrelevant for cell behavior [42,43]. By using our *in silico* model, we therefore analyzed whether strain fields were overlapping using a threshold of 0.5% strain (Fig. 6A). For a distance of 50 μm, strain fields were still overlapping (Fig. 6A, panel I). This indicates that cells were close enough to communicate with each other purely mechanically. This cell-ECM-cell mechanical communication has been introduced with the term paratensile signaling recently [44]. To test whether such paratensile signaling explains the enhanced BMP-2 response, we reduced the cell seeding density to 500 cells/μl, which corresponds to an average intercellular distance of 152 μm. According to the simulations, such a distance results in a strongly reduced mechanical connection between cells for a threshold value of 0.5% (Fig. 6A, panel II). Unexpectedly, we found the same increase in the BMP response in the soft scaffolds compared to the stiff scaffolds at this low cell density as observed for the high cell concentration (Fig. 6B and C). This indicated that an important aspect of the cell behavior leading to the observed increase in BMP-2 signaling in the soft scaffold environment had been overlooked so far.

As the strong deformation of the walls in the soft compared to the stiff scaffolds was in clear agreement with the increased BMP-2 response (Fig. 5D vs. 2C), we first validated whether scaffold wall movement decreased with decreasing cell density. However, even though we observed a reduction both in the velocity of scaffold wall movement (Fig. 6C) as well as in the deformation magnitude (Fig. 6D), the values only decreased by a factor of 1.6 in the softest scaffold, which is much less than would be expected with a 10-fold reduction in seeding density.

To better understand this surprising result, we investigated the dynamic interaction of the cells with the biomaterial in more detail. Using time lapse recordings, we found that the velocity of cell migration was almost twice as high at low cell density compared to high cell density with no discernible effect of the macroscopic biomaterial stiffness on cell velocity (Fig. 6E). Based on the time lapse recordings we hypothesized that the cells did not migrate faster in general, but that the proportion of fast-migrating cells was higher. Thus, we analyzed the frequency distribution of the migration speed of all cells. A double peak distribution at the high cell density indicated that in fact the cells did not behave as a homogeneous population, but were actually composed of a fast and a slow migrating fraction (Fig. 6F). Reducing the cell density in the biomaterial did not reduce the overall distribution profile, but specifically diminished the slow-migrating fraction. Conversely, increasing cell density did not result in more rapidly migrating, motile cells, but rather filled the material with more static cells that did not significantly change their position within the biomaterial over time. Based on the relatively small reduction of biomaterial deformation velocity and magnitude, we concluded that the highly motile cell fraction contributed over-proportionally to the dynamic biomaterial deformation. The described behavior was independent of biomaterial stiffness, indicating a general cell behavior in porous biomaterials.

In order to further validate the interaction between migrating cells and local biomaterial deformation, we monitored material movement as a function of local cell density over time for individual areas (Fig. 6G). We observed that the biomaterial strain is high when a cell is close to the reference position on the scaffold wall. The strain disappeared when the cell had moved away and the distance increased, while it increased again when the cell approached the reference position again. Such events were observed for individual cells, suggesting that material

deformation does not require the collective activity of multiple cells. Our data also show that with very few cells involved, the baseline level of wall movement is low, but peaks as cells approach or move near a specific reference position. When more cells are involved (Supplementary Fig. 6E), the baseline level of movement is higher, but with less pronounced peaks. The data additionally demonstrated that such stronger wall deformations do not occur homogenously throughout the biomaterial and not for each individual cell, which further underlines the strong local mechanical heterogeneity of the material that is experienced by the cells.

In summary, our data demonstrate that enhanced BMP signaling is maintained even at low cell density and can be attributed to the interaction of migrating cells with the non-linear deformation properties (strain stiffening) of the biomaterial scaffold walls. A low cell density is representative of an early stage of tissue healing where highly motile cells would invade the implanted biomaterial. Due to the nonlinear deformation behavior of the scaffold walls, the establishment of traction forces is impeded, as it is the case for substrates that are extrinsically deformed, e.g. during mechanical loading of biomaterials or tissues. As the cell density in the biomaterial increases, more and more cells are in a migratory inactive state where, according to our *in silico* predictions, they are capable to experience deformations induced by the more active cell fraction due to their close proximity. Consequently, both, the autologous cellular mechanical stimulation of individual cells interacting with the scaffold walls and the intercellular stimulation transmitted through the scaffold walls are proposed to be relevant for the observed BMP effect, which can be observed independent of the cell density.

3. Discussion

In this study, we provide evidence that the architecture and mechanical heterogeneity of a soft biomaterial niche has the potential to enable autologous and intercellular mechanical stimulation of cells. This finding has implications not only for growth factor signaling, exemplified here for BMP2, but also for fundamental processes such as biomaterial design, mechanotransduction and metabolism (Fig. 7). The soft and particularly mechanically heterogeneous nature of the biomaterial, comparable to fracture hematoma (2–4 kPa) [45,46] or early granulation tissue (<18 kPa) [47] created a mechanically challenging environment in which cells oscillate between deformable and rigid regions. While many TE strategies e.g. for bone regeneration aim to reproduce the properties of mature tissue with uniformly stiff properties to their adhering cells [48], the here proposed mechanisms would not be available in such material niches. Specifically, the growth factors essential for endogenous regeneration such as BMP-2 seem to be more potent in environments of soft nature mimicking non-mature tissues. Current biomaterial strategies that aim at enabling endogenous regeneration ignore this self-stimulating effect of neighboring cells in early tissue self-assembly.

Harvesting the here presented cell-material interactions and their influence on cell signaling could be of importance to develop more effective biomaterials for bone tissue regeneration by exploiting the intrinsic potential of an amplified growth factor response of cells in tailored 3D environments. In this context, our finding that not all cells interact in the same way with the surrounding material but can be separated into sub-groups with different migratory potentials with associated characteristics in cell-material interaction is of high relevance. It was recently demonstrated that during migration, strain-induced stiffening occours around the leading edge of cells [49] which suggests that this highly migratory sub-population indeed is mostly responsible for the occurring deformation and thus could co-stimulate resting cells in the vicinity of the induced displacement field. The range of these displacement fields thereby depends on the degree of alignment and the directionality of applied forces [50]. Also, our simulations could demonstrate that the quasi-2D character of the scaffold walls leads to a greater extension of displacement fields compared to
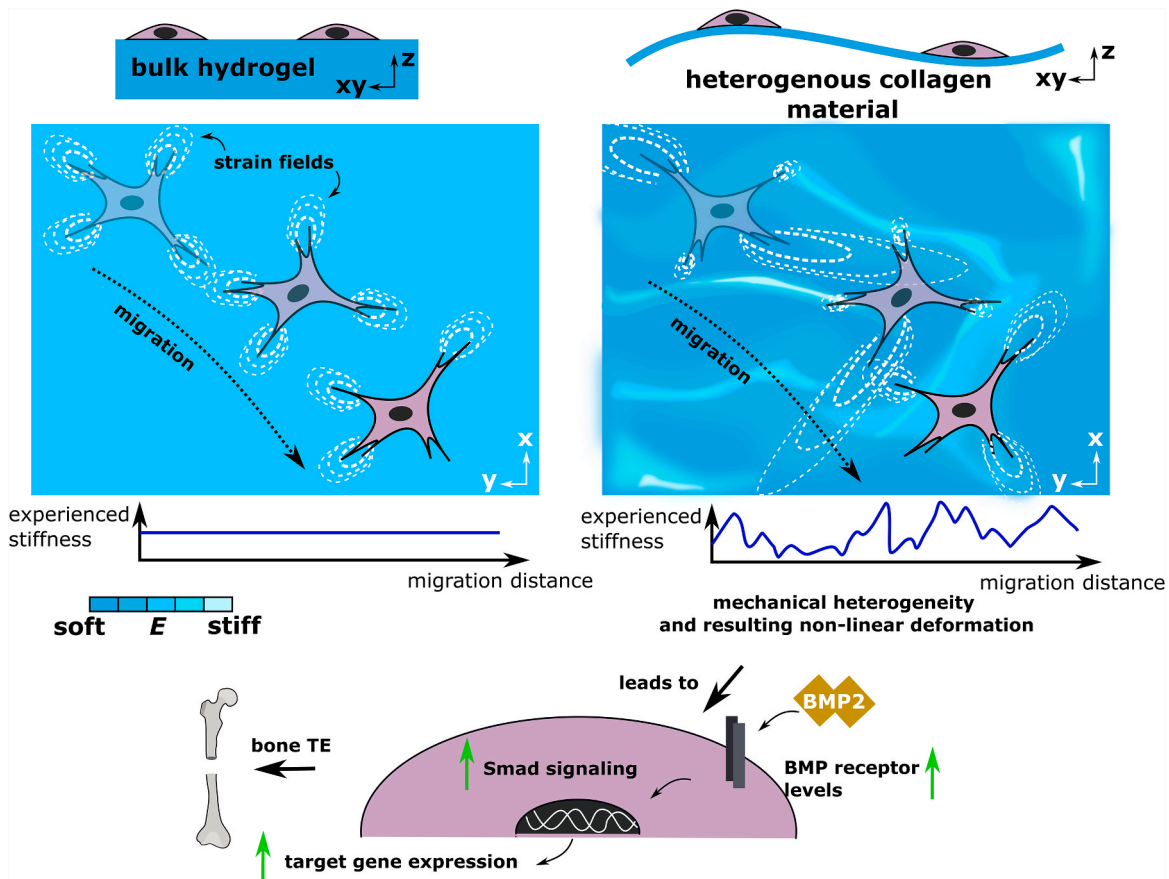
Fig. 7. Cell-to-cell mechanical communication enhances BMP signaling with perspectives for bone TE. While bulk hydrogels are experienced uniformly stiff or soft in all directions, cell experience a high mechanical heterogeneity on sheet-like materials during migration. This resembles a mechanically challenging environment forcing cells to continuously adapt their cytoskeletal tension. This is linked to increased levels of BMP type I receptor and higher BMP2 signaling response which might inspire the development and optimization of such materials for bone TE, e.g. the treatment of large bone defects.

homogenous 3D gels where dissipation in all three dimensions occurs. Longer cultivation of tissue-forming cells finally results in the formation of an intrinsically pre-tensioned, highly aligned fibrous collagen network which is then expected to amplify the strain transmission potential compared to the raw collagen scaffold [45].

Studies have already reported on the mechanical communication of cells via the extracellular matrix which is named as paratensile signaling [44]. In the context of tissue healing, such paratensile signaling was shown to drive fibrosis through myo-fibroblast activation and mechanical recruitment of macrophages [51,52]. Our data suggest that such mechanical cell-ECM-cell communication might play a role in regulating the sensitivity towards BMP growth factors through the regulation of BMP receptor levels at high cell densities while the interaction of individual cells with the heterogeneous mechanical environment and the resulting autologous self-stimulation dominates at lower cell densities. As BMPs are part of the TGF-β superfamily, it can be speculated that not only BMP but also TGF-β receptors are regulated by these cell-material interactions. Thus, consequences of altered signaling might not only support regenerative processes but might, in very soft environments (<1 kPa) that have particular tension-transmitting properties, also contribute to the establishment of a myo-fibroblast phenotype during fibrosis.

The increase in BMP signaling response as a result of cell-induced biomaterial deformation in our scaffold system strongly corresponds to the effect of external mechanical loading that has been shown to increase BMP pathway activation *in vitro* and BMP-mediated bone regeneration *in vivo* [16,17]. While in the context of BMP signaling, the effect of mechanical loading on the signaling is well described, extrinsic

mechanical forces are known to trigger the release of active TGF-β from their matrix-bound latent peptide [53]. In this context, the potential alteration of TGF-β growth factor responsiveness in mechanically stimulating matrix environments (e.g. with heterogeneous deformation properties) might be a relevant modulator of mechanical tissue maturation and eventually fibrosis.

From a clinical perspective, our work highlights the importance of selecting appropriate 3D model systems to study cell behavior when developing therapeutic biomaterial strategies, as key cell responses may differ significantly from results obtained when using structurally and mechanically homogeneous hydrogels. This was particularly visible for LaminA signals, YAP nuclear ratio, but also myosin light chain and overall metabolic activity. While the observations described in this study at first appear to be a unique feature of the employed collagen-based scaffold material, we propose that other materials fulfilling certain mechanical or architectural requirements are equally suitable. In fact, other bio-polymers such as fibrin but also synthetic bio-polymer networks exhibit a non-linear stiffening under strain. The implementation of mechanical heterogeneity into such networks might provoke similar effects as observed here.

The low material stiffness, which is crucial for the intrinsic mechanical self-stimulation of cells and the enhanced growth factor signaling in our study, seems to contradict the mechanical requirements for the *in vivo* application of such materials. Extensive material deformation due to tissue forces is likely to compromise the geometric requirements for successful healing in very soft materials [30]. This is a key argument for using mechanically more competent materials such as hydroxyapatite or titanium on the tissue scale. Hence, the combination

of a mechanical support structure with a soft material niche could be used to achieve more effective tissue healing by addressing both, cell and tissue scale mechanical requirements for successful healing.

4. Conclusion

In summary, this study provides first evidence how soft biomaterial niches with tissue-like heterogeneous mechanical properties can be employed to enhance endogenous growth factor signaling - exemplarily shown here for BMP2. The observed amplification of growth factor responsiveness that results from the dynamic mechanical interaction of cells with their environment, is suggested to be an essential mechanism supporting endogenous healing cascades. Engineering biomaterials that feature such properties in an optimized way would potentially offer a more safe and cost-effective approach to control biochemical signaling cascades such as the here analyzed BMP-2 stimulation for therapeutic purposes.

5. Material & methods

5.1. Cell culture

Human fetal osteoblasts (hFOB 1.19, ATCC® CRL-11372™) were cultured in Dulbecco's Modified Eagle Medium/Nutrient Mixture F-12 (DMEM/F12, Thermo Fischer #11320033) supplemented with 10 vol.-% FBS Superior (FBS, #S 0115; Biochrom AG), 1 vol.-% Penicilin/Streptomycin (P/S, # A 2213; Biochrom AG) and 0.3 mg/ml Geneticin disulphate (G418; #CP11.3, Carl Roth) at a permissive temperature of 34 °C with 5% CO_2 in a humidified incubator. HFOBs were passaged every 3–4 days using 1x Trypsin/EDTA (# 59418C, Sigma Aldrich).

BREluc-C2C12 were cultivated in Dulbecco's Modified Eagle Medium (low glucose, Sigma Aldrich #D5546) supplemented with 10 vol.-% FBS Superior, 1 vol.-% GlutaMAX (Thermo Fischer, #35050-038) and 0.5 mg/ml G418 at 37 °C with 5% CO_2 in a humidified incubator. Cells were passaged every 2–3 days using 1x Trypsin/EDTA.

Primary human mesenchymal stromal/stem cells isolated from human bone marrow of patients undergoing total hip replacement were used in passages 3–4. Cells were cultured in Dulbecco's modified Eagle's medium (DMEM, Sigma Aldrich, #D5546) supplemented with 10 vol.-% FBS Superior, 1 vol.-% GlutaMAX™ and 1 vol.-% P/S at 37 °C with 5% CO_2 in a humidified incubator.

5.2. Scaffold fabrication

Optimaix © macro-porous, porcine collagen I/III scaffolds (Matricel GmbH) were fabricated by a directional freeze-drying method as described previously [32]. In brief: collagen was isolated from porcine skin by mechanical processing to create a dispersion of insoluble collagen fibers of varying thickness and length. The solid content can be varied between 0.5 wt% and 3.0 wt%. The dispersion is then subjected to a directional freezing process that leads to the growth of finger-like ice crystals that causes a phase separation of the insoluble fraction (collagen fibers) from the water compacting the collagen material into thin sheets in between growing crystals. Freeze-drying and EDC-NHS crosslinking chemistry result in blocks of oriented collagen sponges which were processed into thin sheets of 30x40 × 3mm. Sheets were sterilized by gamma-irradiation before use. Cylindrical biopsy punches of 5 mm diameter were used to prepare individual samples of defined size.

5.3. Scaffold seeding

Cylindrical scaffolds were prepared by using a biopsy punch (5 mm Ø) and seeded by dip in uptake from a concentrated cell suspension (5000 cells/μl). The cells were allowed to adhere to the carrier material by incubation at 37 °C without additional medium for 1 h. Scaffolds were then immersed in a reservoir of fresh medium to remove non-adhering cells and transferred into a well plate with expansion medium. Cells were cultivated for 2 days in expansion medium before stimulation.

5.4. BMP2 stimulation

Prior to stimulation, cells were starved for 3 h with reduced or no supplementation of FBS depending on the stimulation time. Smad phosphorylation was analyzed in 0% FBS containing medium, and gene expression was analyzed in medium either containing 0.5% FBS (6 h) or 2% FBS (3 days). E. coli-derived recombinant human BMP2 was received from Prof. Thomas Mueller (Universität Würzburg).

5.5. Western Blotting

Lysates were prepared using 1x RIPA buffer (CST, #9806) according to the manufacturer's instructions. Prior to loading onto polyacrylamide gels, lysates were mixed with 4x Protein sample loading buffer (Li-Cor, #928–40004) and heated to 85 °C for 5 min. SDS polyacrylamide gel electrophoresis was performed using the NuPAGE® electrophoresis system (Thermo Fischer) including 4–12% Bis-Tris gels (Thermo Fischer, # NP0336BOX) and MES SDS Running Buffer (Thermo Fischer, #NP0002) according to the manufacturer's instructions until sufficient separation was achieved. Proteins were transferred onto nitrocellulose membranes (GE Healthcare, #10600002) using the XCell II™ Blot Module (Thermo Fischer) in Transfer buffer (25 mM Tris Base, Sigma Aldrich, #T1503; 192 mM glycine, Carl Roth, #T873; 20 vol.-% methanol, Carl Roth, #0082) for 1 h at 30 V constant. Membranes were washed once in 1x TBS (136 mM NaCl, Merck Milipore, #567440; 15 mM Tris-HCl, Sigma Aldrich, #10812846001, pH7.6) and blocked in 5% BSA/TBS (Carl Roth, # 8076.2). Primary antibodies were applied according to the manufacturer's instructions (pSmad1/5/9, Cell Signaling, #13820; pSmad1/5, Cell Signaling, #9516; GAPDH, Cell Signaling, #2118; pMLC, Cell Signaling, #3675). Membranes were washed three times with TBS-Tween® 20 (0.1%, Carl Roth, # 9127.1) and secondary antibodies (Li-Cor, #925–32211, #925–68070) were incubated for 2 h in 3% BSA/TBS-T. After three consecutive washes with TBS-T, membranes were scanned using the Odyssey Infrared Imaging System (Li-Cor). Signals were quantified inside Odyssey Imaging System software by manual contouring of the respective lanes. Raw intensities were normalized to GAPDH signals of each sample of the same gel.

5.6. Gene expression analysis

RNA was isolated from scaffold samples using the PureLink® RNA Mini Kit (Thermo Fischer, 12183018A) in combination with PureLink® DNase (Thermo Fischer, 12 185 010) to digest genomic DNA according to the manufacturer's instructions. Isolated RNA was reverse transcribed using the iScript™ cDNA Synthesis Kit (Bio-Rad, #170–8891) according to the manufacturer's instructions. Quantitative PCR was performed inside an iQ™5 Real-Time PCR Detection System (Bio-Rad) using iQ™ SYBR® Green Supermix (Bio-Rad, 170–8882). Fold changes were calculated according to the $\Delta\Delta C_T$-method [54] with correction for the primer efficacy as described previously [55]. As housekeeping gene Hypoxanthine-guanine phosphoribosyl transferase 1 (HPRT1) was used. All primer sequences are summarized in Supplementary Table 1.

5.7. Time lapse live-cell microscopy

Cells were seeded as described and stained using CellTracker™ Green CMFDA Dye (Thermo Fischer, #C7025) according to the manufacturer's instructions after 2 days of culture. Scaffolds were transferred into a custom-made incubation chamber and mounted on top of a confocal microscope (see confocal imaging). Images were recorded with a voxel resolution of 1.21x1.21 × 4μm (xyz) at a 30 min time interval.

Recorded data were transferred into binary images and analyzed using the TrackMate ImageJ plugin [56] for absolute movement. For calculations of scaffold straining, the movement of landmarks was quantified by manual tracking using mTrackJ ImageJ plugin. To account for noise-induced tracking error and stage drift, a scaffold of each stiffness was imaged without cells and the mean of the detected movement across all three stiffnesses was subtracted as background signal from all values.

The calculation of cell proximity (both wall-cell and cell-cell) was based object counting within a circular ROI of a radius of 150 μm from the landmark position or an individual cell position, respectively. As straining is a relative expression of deformation between two landmarks, the proximity was calculated relative to the center of a straight line connecting both points. All counts were normalized to the event at a single time point that yielded the maximum of observable cells within the ROI across all experiments and conditions. The maximum hereby received a value of 1. A value of 0 reflects a complete lack of cells within a radial distance of 150 μm.

5.8. Luciferase reporter gene assay

For determining the activity of soluble BMP2 in medium over time, 5 nM BMP2 was incubated in stimulation medium (0% FBS) in a cell culture well plate either without or with a standard cylindrical scaffold sample following the same principles as for stimulation of cells. An aliquot of medium was snap frozen right after mixing to serve as reference. At the respective time points, an aliquot of medium was harvested and snap frozen.

BREluc-C2C12 reporter cells [57] were seeded at a density of 13 000 cells/cm^2. The next day, the cells were washed once with PBS and starved for 8 h in DMEM supplemented with 0.1 vol.-% FBS Superior and 1 vol.-% GlutaMAX™. The conditioned media were thawed, added to the cells and stimulated for an additional 16 h. After that, the cells were washed once with PBS and lysed with 1x of lysis buffer of the luciferase assay system (Promega, #E1500) according to the manufacturer's instructions. The luminescent signal was recorded using an infinite 200Pro plate reader (Tecan).

5.9. PDMS stiffness substrate fabrication

PDMS substrates of varying stiffness were fabricated with Sylgard 184 (Dow Corning) in a 1:30 (stiff) and 1:70 (soft) ratio of base and crosslinker. The mixture was poured into multi-well plates and crosslinked at 70 °C for 10 h. Plates were sterilized with 70% Ethanol and treated over night with 0.1 mg/ml dopamine in 10 mM Tris HCl (pH 8.5) [58]. Substrates were coated with 20 μg/ml collagen [Collagen A, Sigma Aldrich, L7220] for 30 min at 37 °C before seeding with hFOBs at a density of 20 000 cells/cm^2. Cells were pre-cultivated for 48 h before BMP2 stimulation (see section above).

5.10. PAAm stiffness substrate fabrication

PAAm substrates were prepared according to protocols for coverslip activation described before [59]. Stiffness PAAm gels of defined stiffness were prepared as described before [34]. Gels were coated with 5 μg/cm^2 collagen [Collagen A, Sigma Aldrich, L7220] by covalent crosslinking using UV-activated Sulfosuccinimidyl-6-(4′-azido-2′-nitrophenylamino) hexanoate [Sulfo-SANPAH, Thermo Fischer, 22 589] at a concentration of 1 mg/ml and irradiation of 2 × 200s at 10 mW/cm^2 of 365 nm UV light. Substrates were washed at least 5x for at least 15 min with PBS before seeding with hFOBs in expansion medium at a concentration of 20 000 cells/cm^2. Cells were pre-cultivated for 48 h before BMP2 stimulation (see section above).

5.11. Collagen gel substrate preparation

Collagen gels were prepared from the same collagen dispersion used

for scaffold manufacturing, sieved through a 5 μm mesh to remove large collagen fibers and to prepare a homogeneous dispersion. An approximately 500 μm thick film was smeared on cover glass substrates (Diameter 20 mm) and allowed to dry at ambient temperature. Subsequently, films were either dried in a dehydrator (<30% relative humidity) at room temperature (soft gels) or dried and additionally crosslinked for 24 h at 100 °C under vacuum (stiff substrates). Gels were sterilized by dipping into 70% ethanol followed by a washing step in PBS before being used for cell culture or AFM characterization.

5.12. Concave cell culture chip fabrication

Chips were fabricated with PDMS using a previously described molding process [60]. In brief: Concave spherical substrates were casted with Sylgard 184 (Dow Corning) in a 1:10 ratio using a micro-machined brass mold. The radii of the spheres were designed with a diameter of 100, 200, 300, 400 600, 800 and 1000 μm which corresponds to a curvature of κ = 1/r of: 1/50, 1/100, 1/150, 1/200, 1/300, 1/400 and 1/500 μm^{-1}. PDMS substrates were treated over night at room temperature with 0.1 mg/ml dopamine in 10 mM Tris HCl (pH 8.5) [58]. Substrates were further coated with 20 μg/ml collagen [Collagen A, Sigma Aldrich, L7220] for 30 min at 37 °C. Substrates were finally seeded with hFOBs at a density of 25 000 cells/cm^2 and pre-cultivated for 48 h. Cells were then starved in medium containing 0% FBS for 3 h and stimulated with 5 nM BMP2 for 60 min before fixation using 4% PFA solution. The samples were further stained and imaged (see IF staining & Confocal imaging) and analyzed (see Image Analysis) accordingly.

5.13. If staining & confocal imaging

As described in the section for chondrogenic differentiation, samples were fixed with 4% PFA solution and the reaction was quenched with 25 mM ammonium chloride/PBS. Samples were further cut in halves and a plain surface was prepared by removing 100–200 μm in 10 μm increments using a cryostat (LEICA CM3050S) with samples embedded in Tissue-Tek* O.C.T. Compound. After extracting from the cryo-protective medium, samples were permeabilized with TBS-T 0.1% (50 mM Tris-HCl, Sigma Aldrich, #10812846001; 150 mM NaCl, Merck Milipore, #567440; Triton™ X-100, Sigma Aldrich, #T8787) and blocked with 1 wt.-% BSA/5 vol.-% normal donkey serum (Abcam, #ab7475)/TBS. Primary antibodies (YAP, Cell Signaling, #14074; LaminA, Abcam, #ab8980; pSmad1/5/9, Cell Signaling, #13820) were incubated according to the manufacturer's instructions in antibody diluent (Agilent, S302283-2). Secondary antibodies (Thermo Fischer, A-21206) and actin labelling dyes (Phalloidin, Thermo Fischer, #A22284 and Sigma Aldrich, #19083) were diluted in blocking solution. Nuclear staining was performed with Draq5 (Biolegend, #424101) or SYTOX™ Green (Thermo Fischer, #S7020).

Images were recorded with a Leica SP5 II confocal laser scanning microscope equipped with a 25x (time-lapse live-cell imaging, curved substrates) 40x (cell morphology & mechanosensation marker) and 63× (scaffold wall thickness) water immersion objectives. The second harmonic generation signal of the scaffold was generated using a Spectra Physics Ti:Sapphire laser (Mai Tai HP) at 910 nm wavelength.

5.14. Image Analysis

5.14.1. Analysis of scaffold architecture

The pore spanning distance was analyzed in top view (orthogonal to pore direction, Fig. 1C, top panel) using ImageJ by manual measurement of the distance between two parallel walls. The density of stabilizing struts was calculated by manual counting with normalization to the volume of the recorded stack. The wall thickness was measured using the BoneJ plugin of high resolution scans [33].

5.14.2. Cell morphology

Representative images were created using the Imaris software. The cell morphology was quantified with ImageJ using maximum projections.

5.14.3. YAP nuclear/cytosolic ratio

The mean YAP signal of nuclear (based on DAPI signal) or cytosolic (based on actin signal with nucleus excluded) ROIs was quantified from maximum projections and a ratio was formed for each image. At least 5 images at different positions were taken per experiment.

5.14.4. LaminA signal

A sum projection of LaminA was created and a nuclear stain was applied as a mask to clear non-nuclear signals. The sum histogram was divided by the nuclear object count to derive a signal/cell for each image. At least 5 images at different positions were taken per experiment.

5.14.5. Nuclear pSmad

A nuclear ROI mask was generated from nuclear DNA staining. Next, a sum projection was created and the nuclear pSmad signal was calculated by summing up all pixel values within the nuclear ROI mask of each cell. Signals were directly normalized to the mean signal of all cells that were detected on the flat region around each sphere for each image. The mean was then formed of all normalized signals for each sphere.

5.14.6. Actin signal co-localization

Co-localization of cellular actin signal either with collagen walls or wall-interconnecting struts was performed by creating a threshold mask for actin, collagen struts and collagen walls. Struts were separated from collagen walls by manual contouring before converting into a separate mask. The overlay either of actin and collagen wall or actin and strut masks was used to measure the amount of actin area localizing to these structural elements. The remaining signal that not co-localized with either of the collagen signal masks was considered as spanning. To avoid false negative or positive signals, co-localization was only quantified in side view with clear pore geometry visible and across a maximum z-depth of 52 μm. A median filter of 2 pixel ensured a dilation of the collagen signal before thresholding to cover proximal actin signal.

5.15. Metabolomics

5.15.1. Cell culture harvest and extraction

Scaffolds were flushed with 10 mM HEPES (pH 7.4), 140 mM NaCl + 3.14 g/L glucose + 10 mM glutamine, dry-soaked and lysed with 500 μL 50% methanol in water containing 2 μg/mL cinnamic acid as internal standard. Samples were snap-frozen, thawed and centrifuged through a filter tip to harvest the whole lysis volume. For each sample, 3 scaffolds were pooled. After the harvest, 1 mL of $CHCl_3$, 0.25 mL of MeOH and 0.25 mL of H_2O were added to the methanolic cell extracts, which were shaken for 60 min at 4 °C and centrifuged at 4149×*g* for 10 min to separate the phases. The polar phase (0.75 mL) was collected and dried at 30 °C at a speed of 1550×*g* at 0.1 mbar using a rotational vacuum concentrator (RVC 2–33 CDplus, Christ). The samples were pooled after extraction and used as a quality control sample to test the technical variability of the instrument (n = 4, Supplementary Table 3). They were prepared alongside the samples in the same way. After the collection of the polar phases, proteins were extracted for each sample by the addition of 6 mL of 100% MeOH, followed by centrifugation at maximum speed for 10 min. The supernatant was carefully discarded. The pellet was air dried and used for total protein lysis and protein determination.

5.15.2. GC-MS metabolomics measurement of key central carbon pathway metabolites

All the polar cell extracts were stored dry at −80 °C until analysis. The extracts were removed from the freezer and dried in a rotational vacuum concentrator for 60 min before further processing to ensure there was no residual water which may influence the derivatization efficiency. The dried extracts were dissolved in 15 μL of methoxyamine hydrochloride solution (40 mg/mL in pyridine) and incubated for 90 min at 30 °C with constant shaking, followed by the addition of 50 μL of N-methyl-N-[trimethylsilyl]trifluoroacetamide (MSTFA) and incubated at 37 °C for 60 min. The extracts were centrifuged for 10 min at 18 213×*g*, and aliquots of 25 μL were transferred into glass vials for GC-MS measurements. An identification mixture for reliable compound identification was prepared and derivatized in the same way, and an alkane mixture for a reliable retention index calculation was included [1]. The metabolite analysis was performed on a Pegasus 4D GCxGC TOFMS-System (LECO Corporation) complemented with an auto-sampler (Gerstel MPS DualHead with CAS4 injector). The samples were injected in split mode (split 1:5, injection volume 1 μL) in a temperature-controlled injector with a baffled glass liner (Gerstel). The following temperature program was applied during the sample injection: for 2 min, the column was allowed to equilibrate at 68 °C, then the temperature was increased by 5 °C/min until 120 °C, then by 7 °C/min up to 200 °C, then by 12 °C/min up to a maximum temperature of 320 °C, which was then held for 7.5 min. The gas chromatographic separation was performed on an Agilent 7890 (Agilent Technologie), equipped with a VF-5 ms column (Agilent Technologies) of 30 m length, 250 μm inner diameter and 0.25 μm film thickness. Helium was used as the carrier gas with a flow rate of 1.2 mL/min. The spectra were recorded in a mass range of 60–600 *m/z* with 10 spectra/second. Each ample was measured twice (technical replicates). The GC-MS chromatograms were processed with the ChromaTOF software (LECO Corporation) including baseline assessment, peak picking and computation of the area and height of peaks without a calibration by using an in-house created reference and library containing the top 3 masses by intensity for 45 metabolites (58 intermediates; see Supplementary Table 2) related to the central carbon metabolism. Metabolites were considered valid for statistical analysis when they appeared in a minimum of 3 biological replicates (BR). A lower technical variability compared to the biological variability was shown for all three softness types of the scaffolds.

5.16. Data analysis (metabolomics)

The data were exported and merged using an in-house written R script. The metabolites were considered valid when they appeared in a minimum of n = 3 biological replicates. The peak area of each metabolite was calculated by normalization to the internal standard cinnamic acid and additionally to the protein content. Relative quantities were used. To analyze possible contaminations due to the scaffold alone, empty scaffolds were treated and analyzed alongside to the samples. Metabolites were valid when they appeared in a minimum of 3/6 empty scaffolds. The mean peak area of the detected metabolites from the empty scaffolds was subtracted from the peak area of the measured samples. See also Supplementary Tables 2 and 3

5.16.1. Protein determination

The protein amount was determined using the BCA (bicinchoninic acid) assay (Thermo Fischer, #23250) according to the manufacturer's instructions.

5.16.2. Scanning electron microscopy

Scanning electron microscopy of freeze-dried, gold-sputtered collagen scaffolds was performed using the JCM-600 (JEOL GmbH) device.

5.17. Mechanical testing

Calculation of the compressive stiffness (elastic modulus E) was performed by mono-axial compression testing with use of the BOSE

ElectroForce Mechanical Test Instruments TestBench system combined with a Model 31 Low load cell (Honeywell Corp.). Cylindrical samples were compressed in uniaxial direction along the direction of the pores for three repetitive cycles over a displacement of 0.3 and 0.6 mm with a constant speed of 0.05 mm/s. For zero, as well as 0.3 and 0.6 mm compression the position was kept constant for 30 s. Recorded force-displacement curves were transferred to stress (σ)/strain (ε) curves by regarding sample area and height and the elastic modulus was calculated for the linear region of the curve by linear fitting according to:

$$\sigma(y) = E \bullet \varepsilon(x)$$

The values for macroscopic stiffness presented here are indicative for the axial compression direction (along the direction of the pores). Radial stiffness was recently observed to be in the range of 0.2–0.25x the axial stiffness [45].

5.18. Atomic force microscopy

Quantification of the scaffold wall bending stiffness using AFM-based deflection of individual segments of the scaffold walls (Fig. 1H) was performed previously [31] and was re-analyzed here. Briefly, segments of the scaffold walls were prepared by cryo-cutting of the scaffold perpendicular to the pore axis into sections of approximately 20 µm thickness and were mounted between a microscope slide and a cover glass (For details see [31], materials and methods section 2.4). A controlled force of up to 6 nN was applied to the individual scaffold wall cantilevers beams via AFM using a spherical tip with 25 µm diameter. Cantilever beam bending stiffness $k = \frac{F}{d}$ in N/m (F = applied force, d = tip displacement) was analyzed from the slope of the force-distance curves in the linear region. At least 48 scaffold wall cantilever beams were analyzed per scaffold type. Values of bending stiffness obtained from AFM were corrected for the individual cantilever width b and length l (distance between the point of fixation and the point of indentation) according to the cantilever beam bending theory and the moment of inertia for a beam with rectangular cross-section (width b) to obtain a normalized bending stiffness $k_{norm} = k \frac{l^3}{b}$ in N*m.

Force measurements on thin collagen gels were performed using an JPK Bruker Cell Hesion 200 system equipped with a 10 µm spherical tip on a pre-calibrated cantilever (Bruker MLCT-SPH-10UM) with an approach velocity of 3 µm/s and a setpoint of 4 nN. Measurement was performed at 37 °C in phosphate-buffered saline after 24–48 h pre-incubation in cell culture medium at 37 °C. Surface mapping with a 3x3 indentation matrix over 60×60 µm area was performed at multiple distant locations on the gels. Elastic moduli were calculated by fitting force curves with the Hertz model using the JPK Bruker data processing software.

5.19. Finite element model and strain field calculation

Individual walls from the scaffold were modeled according to a previous publication, taking into account their geometrical characteristics and a material elastic modulus of 60 kPa and 705 kPa for the soft and stiff scaffold respectively [REF: 10.1016/j.msec.2019.109760]. Each scaffold wall is composed of at least 174×10^3 S3 elements. In addition, a flat gel-like substrates were modeled presenting elastic moduli in agreement to those experimentally measured for the PPA gel. Each gel-like substrate is composed of at least 684×10^3 C3D4H elements. For both models a Poisson ratio was set to 0.49 to simulate an incompressible material and symmetry boundary conditions were applied. Individual cells were modeled with a circular morphology of 30 µm diameter and were placed forming an array with 50, 100, 150, 200 and 300 µm from each other. The cells were tied to their respective surface and restricted in displacement and rotation (UR = U = 0). Based on previous simulation approaches [38], active cell contraction was modeled simulating a thermal expansion coefficient of 0.001 K^{-1} and a

negative thermal load of 100 K. Each cell is composed of at least 63 S3 elements.

The position of each cell array was rotated on the substrate from 0° to 90° in 15° intervals. The strain field was calculated as the sum of the maximum principle strain along the axis defined by the array of cells, within an area of 1320 µm $\times$ 366 µm (length x width). Data is presented as mean $\pm$ standard deviation for the different cell alignments.

5.20. Statistical analysis & data presentation

Data are presented as mean values with standard deviation of at least 3 independent experiments. Dots indicate single measurements. Box plots are drawn as box for 25% and 75% lower and upper limits overlaid with individual data points. The whisker marks the 1.5x IQR range and minimum and maximum values are indicated as crosses. Data plots were created using the OriginPro 2019b (OriginLab Corporation) or plotted with R (metabolomics data). Significance was tested by Mann-Whitney-U test (two-sided) with Bonferroni's correction for comparison of multiple groups (p* = p x n). Metabolomics data were tested for statistical significance via an unpaired Student's t-test. A value of p or p* <0.05 was considered as statistically significant. Different significant levels are indicated as: #p < 0.1, *p < 0.05, **p < 0.01, ***p < 0.001.

CRediT authorship contribution statement

Erik Brauer: Writing – review & editing, Writing – original draft, Visualization, Validation, Methodology, Investigation, Funding acquisition, Data curation, Conceptualization. **Aaron Herrera:** Writing – review & editing, Methodology, Investigation, Conceptualization. **Raphaela Fritsche-Guenther:** Writing – review & editing, Visualization, Validation, Methodology, Investigation, Formal analysis, Conceptualization. **Sophie Görlitz:** Methodology, Investigation. **Hans Leemhuis:** Resources, Methodology, Investigation. **Petra Knaus:** Writing – review & editing, Supervision, Resources, Project administration, Funding acquisition, Conceptualization. **Jennifer A. Kirwan:** Validation, Supervision, Resources, Formal analysis, Conceptualization. **Georg N. Duda:** Writing – review & editing, Supervision, Resources, Project administration, Funding acquisition. **Ansgar Petersen:** Writing – review & editing, Writing – original draft, Visualization, Validation, Supervision, Resources, Project administration, Methodology, Funding acquisition, Formal analysis, Conceptualization.

Declaration of competing interest

The authors declare that they have no known competing financial interests or personal relationships that could have appeared to influence the work reported in this paper.

Data availability

Data will be made available on request.

Appendix A. Supplementary data

Supplementary data to this article can be found online at https://doi.

org/10.1016/j.biomaterials.2024.122614.

References

[1] P. De Biase, R. Capanna, Clinical applications of BMPs, Injury 36 (Suppl 3) (2005) S43–S46, https://doi.org/10.1016/j.injury.2005.07.034.

[2] O.P. Gautschi, S.P. Frey, R. Zellweger, Bone morphogenetic proteins in clinical applications, ANZ J. Surg. 77 (2007) 626–631, https://doi.org/10.1111/j.1445-2197.2007.04175.x.

[3] P.V. Giannoudis, T.A. Einhorn, Bone morphogenetic proteins in musculoskeletal medicine, Injury 40 (Suppl 3) (2009) S1–S3, https://doi.org/10.1016/S0020-1383(09)00642-1.

[4] V.S. Salazar, L.W. Gamer, V. Rosen, BMP signalling in skeletal development, disease and repair, Nat. Rev. Endocrinol. advance on (2016) 203–221, https://doi.org/10.1038/nrendo.2016.12.

[5] D.O. Wagner, C. Sieber, R. Bhushan, J.H. Börgermann, D. Graf, P. Knaus, BMPs: from bone to body morphogenetic proteins, Sci. Signal. 3 (2010) 1–7, https://doi.org/10.1126/scisignal.3107mr1.

[6] A.W. James, G. LaChaud, J. Shen, G. Asatrian, V. Nguyen, X. Zhang, K. Ting, C. Soo, A review of the clinical side effects of bone morphogenetic protein-2, Tissue Eng., Part B 22 (2016) 284–297, https://doi.org/10.1089/ten.teb.2015.0357.

[7] H.S. Yang, W.-G. La, S.H. Bhang, J.-Y. Jeon, J.H. Lee, B.-S. Kim, Heparin-conjugated fibrin as an injectable system for sustained delivery of bone morphogenetic protein-2, Tissue Eng. 16 (2010) 1225–1233, https://doi.org/10.1089/ten.TEA.2009.0390.

[8] S.S. Lee, B.J. Huang, S.R. Kaltz, S. Sur, C.J. Newcomb, S.R. Stock, R.N. Shah, S. I. Stupp, Bone regeneration with low dose BMP-2 amplified by biomimetic supramolecular nanofibers within collagen scaffolds, Biomaterials 34 (2013) 452–459, https://doi.org/10.1016/j.biomaterials.2012.10.005.

[9] X. He, Y. Liu, X. Yuan, L. Lu, Enhanced healing of rat calvarial defects with MSCs loaded on BMP-2 releasing chitosan/alginate/hydroxyapatite scaffolds, PLoS One 9 (2014), https://doi.org/10.1371/journal.pone.0104061.

[10] H. Zhang, F. Migneco, C.-Y. Lin, S.J. Hollister, Chemically-conjugated bone morphogenetic protein-2 on three-dimensional polycaprolactone scaffolds stimulates osteogenic activity in bone marrow stromal cells, Tissue Eng. 16 (2010) 3441–3448, https://doi.org/10.1089/ten.TEA.2010.0132.

[11] H. Shen, X. Hu, F. Yang, J. Bei, S. Wang, The bioactivity of rhBMP-2 immobilized poly(lactide-co-glycolide) scaffolds, Biomaterials 30 (2009) 3150–3157, https://doi.org/10.1016/j.biomaterials.2009.02.004.

[12] X. Chen, B. Tan, Z. Bao, S. Wang, R. Tang, Z. Wang, G. Chen, S. Chen, W.W. Lu, D. Yang, S. Peng, Enhanced bone regeneration via spatiotemporal and controlled delivery of a genetically engineered BMP-2 in a composite Hydrogel, Biomaterials 277 (2021) 121117, https://doi.org/10.1016/j.biomaterials.2021.121117.

[13] A.J. Engler, S. Sen, H.L. Sweeney, D.E. Discher, Matrix elasticity directs stem cell lineage specification, Cell 126 (2006) 677–689, https://doi.org/10.1016/j.cell.2006.06.044.

[14] O. Chaudhuri, L. Gu, D. Klumpers, M. Darnell, S.A. Bencherif, J.C. Weaver, N. Huebsch, H.-P. Lee, E. Lippens, G.N. Duda, D.J. Mooney, Hydrogels with tunable stress relaxation regulate stem cell fate and activity, Nat. Mater. 15 (2016) 326–334, https://doi.org/10.1038/nmat4489.

[15] M. Werner, S.B.G. Blanquer, S.P. Haimi, G. Korus, J.W.C. Dunlop, G.N. Duda, D. W. Grijpma, A. Petersen, Surface curvature differentially regulates stem cell migration and differentiation via altered attachment morphology and nuclear deformation, Adv. Sci. 201600347 (2016) 1600347, https://doi.org/10.1002/advs.201600347.

[16] J. Kopf, A. Petersen, G.N. Duda, P. Knaus, BMP2 and mechanical loading cooperatively regulate immediate early signalling events in the BMP pathway, BMC Biol. 10 (2012) 37, https://doi.org/10.1186/1741-7007-10-37.

[17] C. Schwarz, C.-E. Ott, D. Wulsten, E. Brauer, S. Schreivogel, A. Petersen, K. Hassanein, L. Roewer, T. Schmidt, B.M. Willie, G.N. Duda, The interaction of BMP2-induced defect healing in rat and fixator stiffness modulates matrix alignment and contraction, JBMR Plus 2 (2018) 174–186, https://doi.org/10.1002/jbm4.10031.

[18] C. Schwarz, D. Wulsten, A. Ellinghaus, J. Lienau, B.M. Willie, G.N. Duda, Mechanical load modulates the stimulatory effect of BMP2 in a rat nonunion model, Tissue Eng. 19 (2013) 247–254, https://doi.org/10.1089/ten.tea.2012.0265.

[19] J. Zhou, P. Lee, C. Tsai, C. Lee, T. Yang, H. Chuang, W. Lin, T. Lin, J. Caramel, P. Goguet-rubio, L.K. Linares, C. De Bettignies, A. Thépot, C. Deraison, K. Chébli, A. Hovnanian, P. Hainaut, P. Dubus, J. Zhou, P. Lee, C. Tsai, C. Lee, T. Yang, H. Chuang, W. Lin, Force-specific activation of Smad1/5 regulates vascular endothelial cell cycle progression in response to disturbed flow, Proc. Natl. Acad. Sci. USA 109 (2012), https://doi.org/10.1073/pnas.1212269109, 14716–14716.

[20] C. da Silva Madaleno, J. Jatzlau, P. Knaus, BMP signalling in a mechanical context – implications for bone biology, Bone 137 (2020), https://doi.org/10.1016/j.bone.2020.115416.

[21] C. Hiepen, P. Mendez, P. Knaus, It takes two to tango: endothelial TGFβ/BMP signaling crosstalk with mechanobiology, Cells 9 (2020) 1965, https://doi.org/10.3390/cells9091965.

[22] M. Reichenbach, P.L. Mendez, C. da Silva Madaleno, V. Ugorets, P. Rikeit, S. Boerno, J. Jatzlau, P. Knaus, Differential impact of fluid shear stress and YAP/TAZ on BMP/TGF-β induced osteogenic target genes, Adv. Biol. 5 (2021), https://doi.org/10.1002/adbi.202000051.

[23] H.L. Ashe, Modulation of BMP signalling by integrins, Biochem. Soc. Trans. 44 (2016) 1465–1473, https://doi.org/10.1042/BST20160111.

[24] S. Schreivogel, V. Kuchibhotla, P. Knaus, G.N. Duda, A. Petersen, Load-induced osteogenic differentiation of mesenchymal stromal cells is caused by mechano-regulated autocrine signaling, J. Tissue Eng. Regen. Med. 13 (2019) 1992–2008, https://doi.org/10.1002/term.2948.

[25] R. Guo, S. Lu, A.R. Merkel, J.A. Sterling, S.A. Guelcher, Substrate modulus regulates osteogenic differentiation of rat mesenchymal stem cells through integrin β1 and BMP receptor type IA, J. Mater. Chem. B 4 (2016) 3584–3593, https://doi.org/10.1039/C5TB02747K.

[26] J. Du, X. Chen, X. Liang, G. Zhang, J. Xu, L. He, Q. Zhan, X.-Q. Feng, S. Chien, C. Yang, Integrin activation and internalization on soft ECM as a mechanism of induction of stem cell differentiation by ECM elasticity, Proc. Natl. Acad. Sci. USA 108 (2011) 9466–9471, https://doi.org/10.1073/pnas.1106467108.

[27] Q. Wei, A. Holle, J. Li, F. Posa, F. Biagioni, O. Croci, A.S. Benk, J. Young, F. Noureddine, J. Deng, M. Zhang, G.J. Inman, J.P. Spatz, S. Campaner, E. A. Cavalcanti-Adam, BMP-2 signaling and mechanotransduction synergize to drive osteogenic differentiation via YAP/TAZ, Adv. Sci. 7 (2020) 1–15, https://doi.org/10.1002/advs.201902931.

[28] B. Trappmann, J.E. Gautrot, J.T. Connelly, D.G.T. Strange, Y. Li, M.L. Oyen, M. A. Cohen Stuart, H. Boehm, B. Li, V. Vogel, J.P. Spatz, F.M. Watt, W.T.S. Huck, Extracellular-matrix tethering regulates stem-cell fate, Nat. Mater. 11 (2012) 642–649, https://doi.org/10.1038/nmat3339.

[29] M. Moncayo-Donoso, G.A. Rico-Llanos, D.A. Garzón-Alvarado, J. Becerra, R. Visser, M.R. Fontanilla, The effect of pore directionality of collagen scaffolds on cell differentiation and in vivo osteogenesis, Polymers 13 (2021), https://doi.org/10.3390/polym13183187.

[30] A. Petersen, A. Princ, G. Korus, A. Ellinghaus, H. Leemhuis, A. Herrera, A. Klaumünzer, S. Schreivogel, A. Woloszyk, K. Schmidt-Bleek, S. Geissler, I. Heschel, G.N. Duda, A biomaterial with a channel-like pore architecture induces endochondral healing of bone defects, Nat. Commun. 9 (2018) 4430, https://doi.org/10.1038/s41467-018-06504-7.

[31] A. Herrera, J. Hellwig, H. Leemhuis, R. von Klitzing, I. Heschel, G.N. Duda, A. Petersen, From macroscopic mechanics to cell-effective stiffness within highly aligned macroporous collagen scaffolds, Mater. Sci. Eng. C 103 (2019) 109760, https://doi.org/10.1016/j.msec.2019.109760.

[32] H. Schoof, J. Apel, I. Heschel, G. Rau, Control of pore structure and size in freeze-dried collagen sponges, Biomed Mater Res 58 (2001) 352–357, https://doi.org/10.1002/jbm.1028.

[33] M. Doube, M.M. Klosowski, I. Arganda-Carreras, F.P. Cordelières, R.P. Dougherty, J.S. Jackson, B. Schmid, J.R. Hutchinson, S.J. Shefelbine, BoneJ: free and extensible bone image analysis in ImageJ, Bone 47 (2010) 1076–1079, https://doi.org/10.1016/j.bone.2010.08.023.

[34] R.S. Fischer, K.A. Myers, M.L. Gardel, C.M. Waterman, Stiffness-controlled three-dimensional extracellular matrices for high-resolution imaging of cell behavior, Nat. Protoc. 7 (2012) 2056–2066, https://doi.org/10.1038/nprot.2012.127.

[35] B.F. Kennedy, M.L. McFetridge, D.D. Sampson, A.J. Engler, B.-N. Vo, K. Bieback, J. L. Young, H. Taylor-Weiner, D.Y. Kim, A.W. Holle, P. Wijesinghe, Y.S. Choi, J. H. Wen, A.R. Lee, J.P. Spatz, W.J. Hadden, Stem cell migration and mechanotransduction on linear stiffness gradient hydrogels, Proc. Natl. Acad. Sci. USA 114 (2017) 5647–5652, https://doi.org/10.1073/pnas.1618239114.

[36] S. Dupont, L. Morsut, M. Aragona, E. Enzo, S. Giulitti, M. Cordenonsi, F. Zanconato, J. Le Digabel, M. Forcato, S. Bicciato, N. Elvassore, S. Piccolo, Role of YAP/TAZ in mechanotransduction, Nature 474 (2011) 179–184, https://doi.org/10.1038/nature10137.

[37] J. Swift, I.L. Ivanovska, A. Buxboim, T. Harada, P.C.D.P. Dingal, J. Pinter, J. D. Pajerowski, K.R. Spinler, J.W. Shin, M. Tewari, F. Rehfeldt, D.W. Speicher, D. E. Discher, Nuclear lamin-A scales with tissue stiffness and enhances matrix-directed differentiation, Science (2013) 341, https://doi.org/10.1126/science.1240104 (80).

[38] A. Elosegui-Artola, R. Oria, Y. Chen, A. Kosmalska, C. Pérez-González, N. Castro, C. Zhu, X. Trepat, P. Roca-Cusachs, Mechanical regulation of a molecular clutch defines force transmission and transduction in response to matrix rigidity, Nat. Cell Biol. 18 (2016) 540–548, https://doi.org/10.1038/ncb3336.

[39] J.S. Park, C.J. Burckhardt, R. Lazcano, L.M. Solis, T. Isogai, L. Li, C.S. Chen, B. Gao, J.D. Minna, R. Bachoo, R.J. DeBerardinis, G. Danuser, Mechanical regulation of glycolysis via cytoskeleton architecture, Nature 578 (2020) 621–626, https://doi.org/10.1038/s41586-020-1998-1.

[40] R. Fritsche-Guenther, C. Zasada, G. Mastrobuoni, N. Royla, R. Rainer, F. Roßner, M. Pietzke, E. Klipp, C. Sers, S. Kempa, Alterations of mTOR signaling impact metabolic stress resistance in colorectal carcinomas with BRAF and KRAS mutations, Sci. Rep. 8 (2018) 1–17, https://doi.org/10.1038/s41598-018-27394-1.

[41] A.J.F. Stops, L.A. McMahon, D. O'Mahoney, P.J. Prendergast, P.E. McHugh, A finite element prediction of strain on cells in a highly porous collagen-glycosaminoglycan scaffold, J. Biomech. Eng. 130 (2008) 1–11, https://doi.org/10.1115/1.2979873.

[42] M. Koike, H. Shimokawa, Z. Kanno, K. Ohya, K. Soma, Effects of mechanical strain on proliferation and differentiation of bone marrow stromal cell line ST2, J. Bone Miner. Metabol. 23 (2005) 219–225, https://doi.org/10.1007/s00774-004-0587-y.

[43] J.L. Martiel, A. Leal, L. Kurzawa, M. Balland, I. Wang, T. Vignaud, Q. Tseng, M. Théry, Measurement of cell traction forces with ImageJ, Methods Cell Biol. 125 (2015) 269–287, https://doi.org/10.1016/bs.mcb.2014.10.008.

[44] Y. Long, Y. Niu, K. Liang, Y. Du, Mechanical communication in fibrosis progression, Trends Cell Biol. 32 (2022) 70–90, https://doi.org/10.1016/j.tcb.2021.10.002.

[45] E. Brauer, E. Lippens, O. Klein, G. Nebrich, S. Schreivogel, G. Korus, G.N. Duda, A. Petersen, Collagen fibrils mechanically contribute to tissue contraction in an in vitro wound healing scenario, Adv. Sci. (Weinheim, Baden-Wurttemberg, Ger. 6 (2019) 1801780, https://doi.org/10.1002/advs.201801780.

[46] S. Lickert, M. Kenny, K. Selcuk, J.L. Mehl, M. Bender, S.M. Früh, M.A. Burkhardt, J.-D. Studt, B. Nieswandt, I. Schoen, V. Vogel, Platelets drive fibronectin fibrillogenesis using integrin αIIbβ3, Sci. Adv. 8 (2022) eabj8331, https://doi.org/10.1126/sciadv.abj8331.

[47] B. Hinz, The myofibroblast: paradigm for a mechanically active cell, J. Biomech. 43 (2010) 146–155, https://doi.org/10.1016/j.jbiomech.2009.09.020.

[48] H. Qu, H. Fu, Z. Han, Y. Sun, Biomaterials for bone tissue engineering scaffolds: a review, RSC Adv. 9 (2019) 26252–26262, https://doi.org/10.1039/c9ra05214c.

[49] S. van Helvert, P. Friedl, Strain stiffening of fibrillar collagen during individual and collective cell migration identified by AFM nanoindentation, ACS Appl. Mater. Interfaces 8 (2016) 21946–21955, https://doi.org/10.1021/acsami.6b01755.

[50] H. Wang, A.S. Abhilash, C.S. Chen, R.G. Wells, V.B. Shenoy, Long-range force transmission in fibrous matrices enabled by tension-driven alignment of fibers, Biophys. J. 107 (2015) 2592–2603, https://doi.org/10.1016/j.bpj.2014.09.044.

[51] P. Pakshir, M. Alizadehgiashi, B. Wong, N.M. Coelho, X. Chen, Z. Gong, V.B. Shenoy, C.A. McCulloch, B. Hinz, Dynamic fibroblast contractions attract remote macrophages in fibrillar collagen matrix, Nat. Commun. 10 (2019) 1850, https://doi.org/10.1038/s41467-019-09709-6.

[52] L. Liu, H. Yu, H. Zhao, Z. Wu, Y. Long, J. Zhang, X. Yan, Z. You, L. Zhou, T. Xia, Y. Shi, B. Xiao, Y. Wang, C. Huang, Y. Du, Matrix-transmitted paratensile signaling enables myofibroblast-fibroblast cross talk in fibrosis expansion, Proc. Natl. Acad. Sci. U. S. A. 117 (2020) 10832–10838, https://doi.org/10.1073/pnas.1910650117.

[53] T. Maeda, T. Sakabe, A. Sunaga, K. Sakai, A.L. Rivera, D.R. Keene, T. Sasaki, E. Stavnezer, J. Iannotti, R. Schweitzer, D. Ilic, H. Baskaran, T. Sakai, Conversion of mechanical force into TGF-β-mediated biochemical signals, Curr. Biol. 21 (2011) 933–941, https://doi.org/10.1016/j.cub.2011.04.007.

[54] M.W. Pfaffl, A new mathematical model for relative quantification in real-time RT-PCR, Nucleic Acids Res. 29 (2001) e45, https://doi.org/10.1093/nar/29.9.e45.

[55] C. Ramakers, J.M. Ruijter, R.H. Lekanne Deprez, A.F.M. Moorman, Assumption-free analysis of quantitative real-time polymerase chain reaction (PCR) data, Neurosci. Lett. 339 (2003) 62–66, https://doi.org/10.1016/S0304-3940(02)01423-4.

[56] J.Y. Tinevez, N. Perry, J. Schindelin, G.M. Hoopes, G.D. Reynolds, E. Laplantine, S.Y. Bednarek, S.L. Shorte, K.W. Eliceiri, TrackMate: an open and extensible platform for single-particle tracking, Methods 115 (2017) 80–90, https://doi.org/10.1016/j.ymeth.2016.09.016.

[57] B. Herrera, G.J. Inman, A rapid and sensitive bioassay for the simultaneous measurement of multiple bone morphogenetic proteins. Identification and quantification of BMP4, BMP6 and BMP9 in bovine and human serum, BMC Cell Biol. 10 (2009) 20, https://doi.org/10.1186/1471-2121-10-20.

[58] Y.J. Chuah, Y.T. Koh, K. Lim, N.V. Menon, Y. Wu, Y. Kang, Simple surface engineering of polydimethylsiloxane with polydopamine for stabilized mesenchymal stem cell adhesion and multipotency, Sci. Rep. 5 (2015) 18162, https://doi.org/10.1038/srep18162.

[59] S. Plotnikov, B. Sabass, U. Schwarz, C.M. Waterman, High-resolution traction force microscopy, Methods Cell Biol. 123 (2014) 367–394, https://doi.org/10.1016/B978-0-12-420138-5.00020-3.

[60] M. Werner, A. Petersen, N.A. Kurniawan, C.V.C. Bouten, Cell-perceived substrate curvature dynamically coordinates the direction, speed, and persistence of stromal cell migration, Adv. Biosyst. 3 (2019) e1900080, https://doi.org/10.1002/adbi.201900080.